Angewandte Chemie
Eine Zeitschrift der Gesellschaft Deutscher Chemiker

Supporting Information

Medium Diradical Character, Small Hole and Electron Reorganization Energies and Ambipolar Transistors in Difluorenoheteroles

S. Mori, S. Moles Quintero, N. Tabaka, R. Kishi, R. González Núñez, A. Harbuzaru, R. Ponce Ortiz, J. Marín-Beloqui, S. Suzuki, C. Kitamura, C. J. Gómez-García, Y. Dai, F. Negri, M. Nakano, S.-i. Kato*, J. Casado**

Electronic Supporting Information

Synthesis and chemical characterization.

General Procedures. All air-sensitive manipulations were carried out under inert nitrogen gas. 1,8-Dibromocarbazole (**3**) was prepared according to literature procedures.[1] Commercially available reagents and solvents were used as received; *N*,*N*,*N*′,*N*′-tetramethylethylenediamine (TMEDA) was dried over 3Å molecular sieves prior to use. For moisture sensitive reactions, super-dehydrated grade hexane, THF, toluene, and CH_2Cl_2 were used. Column chromatography was carried out using SiO_2. Thin-layer chromatography (TLC) was conducted on aluminum sheets coated with SiO_2 60 F_{254}. Melting points (M.p.) were measured with a hot-stage apparatus (LaboACE LC-5060) and are uncorrected. Recycling gel-permeation chromatography (JAIGEL LC-918) was performed with UV detectors using 1H and 2H polystyrene columns eluted with $CHCl_3$. ^1H and ^{13}C NMR spectra were recorded on a JEOL JNM-ECS400 spectrometer at 400 MHz for ^1H and 100 MHz for ^{13}C. HR-ESI-MS and HR-APCI-MS were conducted in positive or negative mode (Thermo Fisher Scientific LTQ Orbitrap XL). Electronic absorption spectra were recorded in a 1 cm cuvette at room temperature

using a JASCO V-670 or JV-550 spectrometer. ESR spectra were recorded using a JEOL JES-FE1XG or JES-TE200 ESR spectrometer. The solutions of samples were placed in ESR tubes and degassed via the freeze–pump–thaw method, before the ESR tubes were sealed.

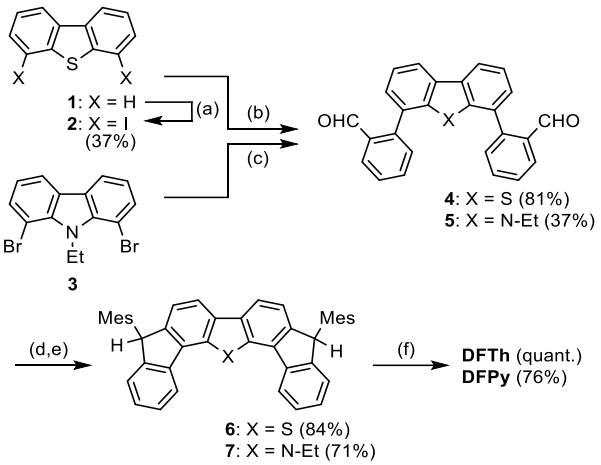

Scheme S1. Synthesis of the studied compounds. *Reagents and conditions:* (a) (i) *n*-BuLi, TMEDA, hexane, 60 °C. (ii) CH_2ICH_2I, rt. (b) 2-formylphenylboronic acid, $Pd_2(dba)_3{\cdot}CHCl_3$, $[(t\text{-}Bu)_3PH][BF_4]$, Cs_2CO_3, THF/H_2O, 70 °C. (c) 2-formylphenylboronic acid, $Pd_2(dba)_3{\cdot}CHCl_3$, SPhos, K_3PO_4, toluene/H_2O. 80 °C (d) MesMgBr, THF, rt. (e) $BF_3{\cdot}Et_2O$, CH_2Cl_2, rt. (f) DDQ, toluene, 80 °C.

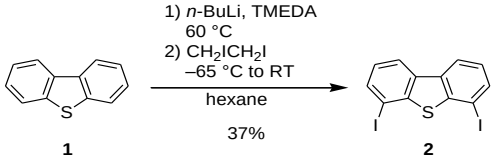

Diiododibenzothiophene 2. To a solution of *N*,*N*,*N*′,*N*′-tetramethylethylenediamine (**1**) (3.70 mL, 24.6 mmol, 3.0 eq.) and hexane (10 mL) was added dropwise a *n*-BuLi (1.55 M solution in hexane, 15.0 mL, 24.6 mmol, 3.0 eq.) at 0 °C under nitrogen atmosphere. The mixture was stirred at 0 °C for 30 min and at room temperature for an additional 30 min. The mixture was then diluted with hexane (15 mL), and dibenzothiophene (1.51 g 5.50 mmol) was added *via* a powder funnel. After heating the mixture at 60 °C for 2 h, the resulting mixture was cooled to −70 °C, and 1,2-diiodoethane (6.92 g, 24.6 mmol, 3.0 eq.) was added. The mixture was stirred at −65 °C for 35 min and at room temperature for an additional 1 h. After addition of aqueous $NaHSO_3$ (10%, 100 mL), the resulting mixture was filtrated, and the organic phase of the filtrate was evaporated under reduced pressure. After the aqueous phase was extracted with CH_2Cl_2 (20 mL × 5), the organic phase was washed with saturated aqueous NaCl (20 mL × 3), dried over anhydrous Na_2SO_4, and evaporated under reduced pressure. After the residue was dissolved with CH_2Cl_2, the solution was passed through a bed of silica gel, and the filtrate was evaporated under reduced pressure. The residue was washed with hexane to give diiododibeonzothiophene **2** (1.33 g, 3.05 mmol, 37%) as a pale brown solid. M.p. 167–169 °C; ^{1}H NMR (400 MHz, $CDCl_3$): δ 8.09 (2H, dd, J = 7.8 & 0.9 Hz), 7.85 (2H, dd, J = 7.8 & 0.9 Hz), 7.23 (2H, t, J = 7.9 Hz); ^{13}C NMR (100 MHz, $CDCl_3$): δ 145.27, 136.37, 126.15, 122.06, 88.13 (5 signals out of 6

expected); UV–vis (CH_2Cl_2): λ_{max}^{abs} (relative intensity) 334 (0.42), 321 (0.34), 308 (sh, 0.23), 289 (0.87), 280 (1.0) nm; HR-APCI-MS (positive): *m*/*z* calcd for $C_{12}H_6I_2S$ 435.82741, found 435.82706 [M^+].

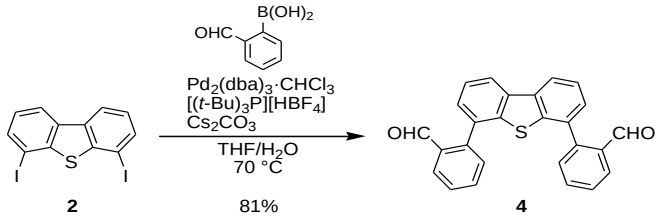

Dialdehyde 4. A solution of diiododibenzothiophene **2** (2.00 g, 4.59 mmol), 2-formylphenylboronic acid (1.65 g, 11.0 mmol, 2.4 eq.), $Pd_2(dba)_3{\cdot}CHCl_3$ (238 mg, 0.230 mmol, 0.05 eq.), [(*t*-Bu)$_3$PH][BF_4] (133 mg, 0.459 mmol, 0.1 eq.), and Cs_2CO_3 (3.29 g, 10.1 mmol, 2.2 eq.) in degassed THF/H_2O (30:1, 110 mL) was stirred at 70 °C for 12 h under nitrogen atmosphere. After addition of H_2O (170 mL), the organic phase was separated and evaporated under reduced pressure, and the aqueous phase was extracted with CH_2Cl_2 (40 mL × 4). The combined organic phase was washed with H_2O (40 mL × 3), dried over anhydrous Na_2SO_4, and evaporated under reduced pressure. The residue was subjected to column chromatography (SiO_2, CH_2Cl_2/hexane 5:1), and the collected material was washed with MeOH to give dialdehyde **4** (1.46 g, 3.73 mmol, 81%) as a white solid. M.p. 227–229 °C; ^{1}H NMR (400 MHz, $CDCl_3$): δ 9.77 (2H, s), 8.29 (2H, dd, *J* =7.9 & 1.1 Hz), 8.05 (2H, dd, *J* = 7.9 & 1.1 Hz), 7.68 (2H, td, *J* = 7.5 & 0.9 Hz), 7.63 (2H, t, *J* = 7.5 Hz), 7.57–7.52 (4H, m), 7.40 (2H, dd, *J* = 7.5 & 0.9 Hz) ; ^{13}C NMR (100 MHz, $CDCl_3$): δ 191.54, 143.69, 140.58, 136.12, 134.41, 133.61, 132.98, 130.55, 129.01, 127.92, 125.29, 121.93 (12 signals out of 13 expected); UV–vis (CH_2Cl_2): λ_{max}^{abs} (relative intensity) 374 (sh, 0.02), 360 (sh, 0.06), 336, (sh, 0.32), 321 (sh, 0.38), 288 (1.0) nm; HR-ESI-MS (positive): *m*/*z* calcd for $C_{26}H_{16}O_2NaS$ 415.07608, found 415.07608 [(M+Na)$^+$].

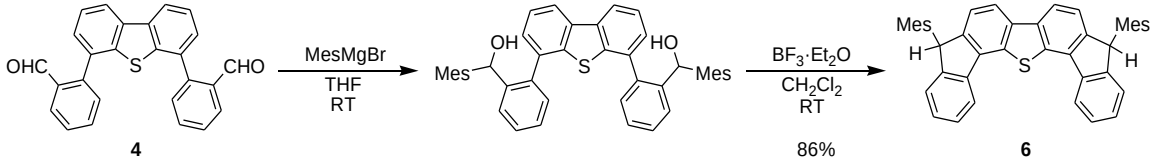

Dihydro DFTh 6. Mesitylmagnesium bromide (1 M solution in THF, 4.52 mL, 4.52 mmol, 6.1 eq.) was added into a THF solution (30 mL) of dialdehyde **4** (295 mg, 0.753 mmol) at room temperature under nitrogen atmosphere, and the resulting solution was stirred for 21 h. After addition of H_2O (30 mL), the organic phase was separated and evaporated under reduced pressure. After the aqueous phase was extracted with CH_2Cl_2 (20 mL × 3), the combined organic phase was washed with H_2O (10 mL × 3), dried over anhydrous Na_2SO_4, and evaporated under reduced pressure. The residue was subjected to column chromatography (SiO_2, CH_2Cl_2/hexane 4:1) to give crude diol (440 mg). To a solution of crude diol (440 mg) in CH_2Cl_2 (50 mL) was added $BF_3{\cdot}OEt_2$ (0.830 mL, 6.79 mmol) at room temperature under nitrogen atmosphere. After the mixture was stirred for 20 min, aqueous $NaHSO_3$ (5%, 160 mL) was added. The organic phase was separated, and the aqueous phase was extracted with CH_2Cl_2 (10 mL × 3). The combined organic phase was washed with H_2O (20 mL × 3), dried over anhydrous $NaSO_4$, and evaporated under reduced pressure to give dihydro DFTh **6** (378 mg, 0.633 mmol, 84%) as a white solid. An analytical sample was obtained by recycling GPC. M.p. 236 °C (decomp.); ^{1}H NMR (400 MHz, $CDCl_3$, diastereomer mixture): δ 8.28 (2H,

d, J = 7.5 Hz), 8.14 (2H, dd, J = 2.8 & 8.0 Hz), 7.63 (2H, t, J = 7.5 Hz), 7.40–7.33 (6H, m), 7.07 (2H, s), 6.67 (2H, s), 5.70 (2H, s), 2.75 (6H, s), 2.30 (6H, s), 1.10, 1.09 (6H, 2s); ^{13}C NMR (100 MHz, $CDCl_3$, diastereomer mixture): δ 147.99, 147.96, 146.54, 146.51, 140.33, 140.31, 138.20, 138.00, 136.66, 135.35, 135.30, 133.77, 132.42, 130.80, 130.78, 129.13, 127.38, 124.29, 124.29, 122.46, 120.96, 120.53, 50, 65, 22.13, 21.15, 18.99, 18.93 (27 signals out of 44 expected); UV–vis (CH_2Cl_2): λ_{max}^{abs} (relative intensity) 265 (1.0), 281 (0.60), 294 (0.66), 306 (0.61), 331 (0.04), 346 (0.03) nm; HR-APCl-MS (positive): m/z calcd for $C_{44}H_{37}S$ 597.26105, found 597.26074 [$(M+H)^+$].

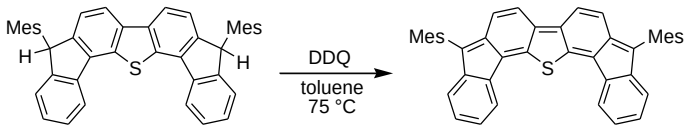

6 quant. **DFTh**

DFTh. To a solution of dihydro DFTh **6** (378 mg, 0.633 mmol) in toluene (55 mL) was added dropwise a solution of 2,3-dichloro-5,6-dicyano-*p*-benzoquinone (DDQ) (260 mg, 1.14 mmol, 1.8 eq.) in toluene (12 mL) at room temperature under nitrogen atmosphere. The solution was stirred at 75 °C for 23 h, and the resulting solution was diluted with toluene. The resulting solution was filtered through a bed of silica gel, and the filtrate was evaporated under reduced pressure to give **DFTh** (332 mg, 0.883 mmol, 88%) as a dark-blue solid. An analytical sample was obtained by recycling GPC. M.p. 246–248 °C; ^{1}H NMR (400 MHz, $CDCl_3$): δ 7.79 (2H, d, J = 7.3 Hz), 7.30 (2H, t, J = 7.3 Hz), 7.18 (2H, d, J = 9.0 Hz), 7.13 (2H, t, J = 7.3 Hz), 7.01 (4H, s), 6.93 (2H, d, J = 7.3 Hz), 6.78 (2H, d, J = 9.0 Hz), 2.38 (6H, s), 2.14 (12H, s); ^{13}C NMR (100 MHz, $CDCl_3$): δ 143.09, 142.39, 138.02, 137.91, 137.73, 137.32, 135.92, 135.18, 133.21, 130.39, 128.38, 127.64, 126.91, 124.55, 123.32, 122.85, 118.63, 21.35, 20.56 (19 signals out of 19 expected), UV–vis (CH_2Cl_2): λ_{max}^{abs} (ε) 278 (62800), 348 (8700), 392 (7400), 414 (7800), 609 (89500), 684 (18100), 743 (11000), 864 (2500) nm; HR-APCI-MS (positive): m/z calcd for $C_{44}H_{35}S$ 595.24540, found 595.24548 [$(M+H)^+$].

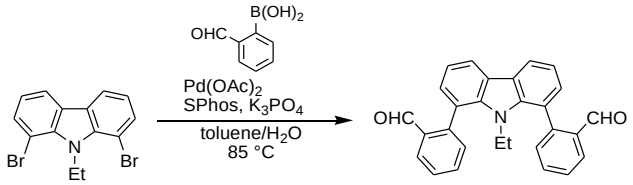

3 **5**

Dialdehyde 5. A solution of dibromocarbazole **3** (476 mg, 1.35 mmol), 2-formylphenylboronic acid (490 mg, 3.24 mmol, 2.4 eq.), $Pd(OAc)_2$ (15 mg, 0.068 mol, 0.05 eq.), 2-dicyclohexylphosphino-2′,6′-dimethoxybiphenyl (SPhos) (57 mg, 0.14 mmol, 0.1 eq.), and K_3PO_4 (1.10 g, 5.18 mmol, 3.8 eq.) in degassed toluene/H_2O (3:1, 100 mL) was stirred at 85 °C for 29 h under nitrogen atmosphere. After addition of H_2O (50 mL), the organic phase was separated, and the aqueous phase was extracted with CH_2Cl_2 (15 mL × 3). The organic phase was washed with H_2O (20 mL × 3), dried over anhydrous Na_2SO_4, and evaporated under reduced pressure. The residue was purified by column chromatography (SiO_2, CH_2Cl_2) to give dialdehyde **5** (202 mg, 0.502 mmol, 37%) as a white solid. M.p.183–185 °C; ^{1}H NMR (400 MHz, $CDCl_3$, atropisomer

mixture): δ 9.84, 9.77 (2H, 2s), 8.22, 8.21 (2H, 2d, J = 7.6 Hz), 8.03, 8.02 (2H, 2d, J = 8.4 Hz), 7.68–7.50 (1H, m), 7.64 (1H, d, J = 7.6 Hz), 7.53 (2H, d, J = 7.6 Hz), 7.53–7.50 (2H, m), 7.37, 7.36 (2H, 2t, J = 7.6 Hz), 7.27–7.24 (2H, m), 3.24, 3.16, 3.03 (2H, 1q & 2sext., J = 7.2 Hz), 0.31, 0.28 (3H, 2t, J = 7.0 Hz); ^{13}C NMR (100 MHz, $CDCl_3$, atropisomer mixture): δ 192.40, 191.96, 144.25, 144.16, 140.52, 140.17, 134.75, 134.47, 134.34, 134.01, 131.43, 131.25, 130.60, 130.49, 128.80, 127.86, 127.68, 126.20, 125.94, 122.34, 120.86, 120.60, 120.48, 40.54, 40.34, 14.68, 14.61 (27 signals out of 30 expected); UV–vis (CH_2Cl_2): λ_{max}^{abs} (relative intensity) 275 (sh, 1.0), 297 (0.85), 277 (sh, 0.32) nm; HR-ESI-MS (positive): m/z calcd for $C_{28}H_{21}O_2NNa$ 426.14645, found 426.14627 [$(M+Na)^+$].

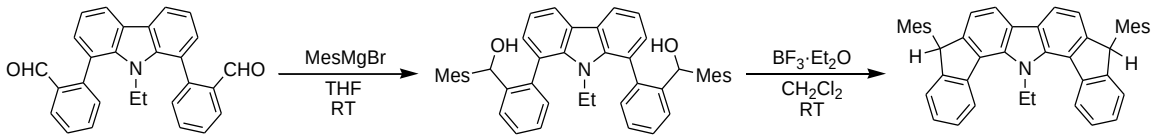

5 71% **7**

Dihydro DFPy 7. Mesitylmagnesium bromide (1 M solution in THF, 8.3 mL, 8.28 mmol, 6.0 eq.) was added into a THF solution (20 mL) of dialdehyde **5** (555 mg, 1.38 mmol) at room temperature, and the resulting solution was stirred for 15 h under nitrogen atmosphere. After addition of H_2O (20 mL), the organic phase was separated and evaporated under reduced pressure. After the aqueous phase was extracted with CH_2Cl_2 (50 mL × 4), the combined organic phase was washed with H_2O (100 mL × 3), dried over anhydrous Na_2SO_4, and evaporated under reduced pressure to give crude diol (941 mg). To a solution of crude diol (941 mg) in CH_2Cl_2 (20 mL) was added $BF_3{\cdot}OEt_2$ (2.00 mL, 14.6 mmol) at room temperature under nitrogen atmosphere. After the mixture was stirred for 30 min, aqueous $NaHSO_3$ (5%, 30 mL) was added. The organic phase was separated, washed with $NaHSO_3$ (5%, 100 mL × 4), dried over anhydrous $NaSO_4$, and evaporated under reduced pressure. The residue was washed with MeCN to give dihydro DFPy **7** (597 mg, 0.941 mmol, 71%) as a white solid. An analytical sample was obtained by recycling GPC. M.p. 261 °C (decomp.); ^{1}H NMR (400 MHz, $CDCl_3$, diastereomer mixture): δ 8.29 (2H, d, J = 7.2 Hz), 7.91 (2H, d, J = 7.7 Hz), 7.58 (2H, td, J = 7.2 & 2.5 Hz), 7.34–7.30 (4H, m), 7.16 (2H, dd, J = 7.0 & 0.8 Hz), 7.06 (2H, s), 6.65 (2H, s), 5.76 (2H, s), 5.00 (2H, q, J = 7.0 Hz), 2.74 (6H, s), 2.30 (6H, s), 0.96 (6H, s), 0.56 (3H, t, J = 7.0 Hz); ^{13}C NMR (100 MHz, $CDCl_3$): δ 148.32, 147.92, 141.72, 140.11, 138.09, 137.97, 136.40, 134.57, 130.69, 128.90, 128.43, 127.32, 126.98, 126.50, 124.34, 123.48, 118.94, 117.85, 50.58, 45.24, 21.96, 21.05, 18.73, 12.31 (24 signals out of 48 expected); UV–vis (CH_2Cl_2): λ_{max}^{abs} (relative intensity) 266 (1.00), 308 (0.87), 353 (sh, 0.12) nm; HR-APCI-MS (positive): m/z calcd for $C_{46}H_{42}N$ 608.33118, found 608.33081 [$(M+H)^+$].

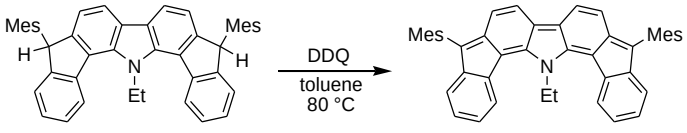

7 76% **DFPy**

DFPy. To a solution of dihydro DFPy **7** (540 mg, 0.888 mmol) in toluene (50 mL) was added dropwise a solution of 2,3-dichloro-5,6-dicyano-*p*-benzoquinone (DDQ) (363 mg, 1.60 mmol, 1.8 eq.) in toluene (20 mL) at room temperature under nitrogen atmosphere. After the solution was stirred at 80 °C for 22 h, the resulting solution was diluted with toluene (100 mL) and filtered through a bed of silica gel. The filtrate was evaporated under reduced pressure to give **DFPy** (420 mg, 0.677 mmol, 76%) as a

bluish-black solid. An analytical sample was obtained by recycling GPC. M.p. 259–261 °C; ^{1}H NMR (400 MHz, $CDCl_3$): δ 7.80 (2H, d, J = 7.1 Hz), 7.19 (2H, d, J = 7.1 Hz), 7.06 (2H, t, J = 7.1 Hz), 7.00 (4H, s), 6.88 (2H, J = 7.1 Hz), 6.88 (2H, J = 8.9 Hz), 6.58 (2H, d J = 8.9 Hz), 4.73 (2H, q, J = 7.0 Hz), 2.38 (6H, s), 2.13 (12H, s), 1.11 (3H, t, J =7.0 Hz); ^{13}C NMR (100 MHz, $CDCl_3$): δ 146.41, 142.71, 142.22, 137.51, 138.43, 137.09, 134.85, 132.67, 130.82, 128.24, 126.23, 124.23, 124.04, 122.61, 120.85, 116.87, 44.98, 21.33, 20.54, 13.61 (20 signals out of 21 expected); UV–vis (CH_2Cl_2): λ_{max}^{abs} (ε) 257 (sh, 0.51), 265 (0.61), 277 (sh, 0.65), 287 (1.0), 302 (0.38), 313 (0.32) nm; HR-APCI-MS (positive): m/z calcd for $C_{46}H_{40}N$ 606.31553, found 606.31549 [$(M+H)^+$].

Chemical characterization.

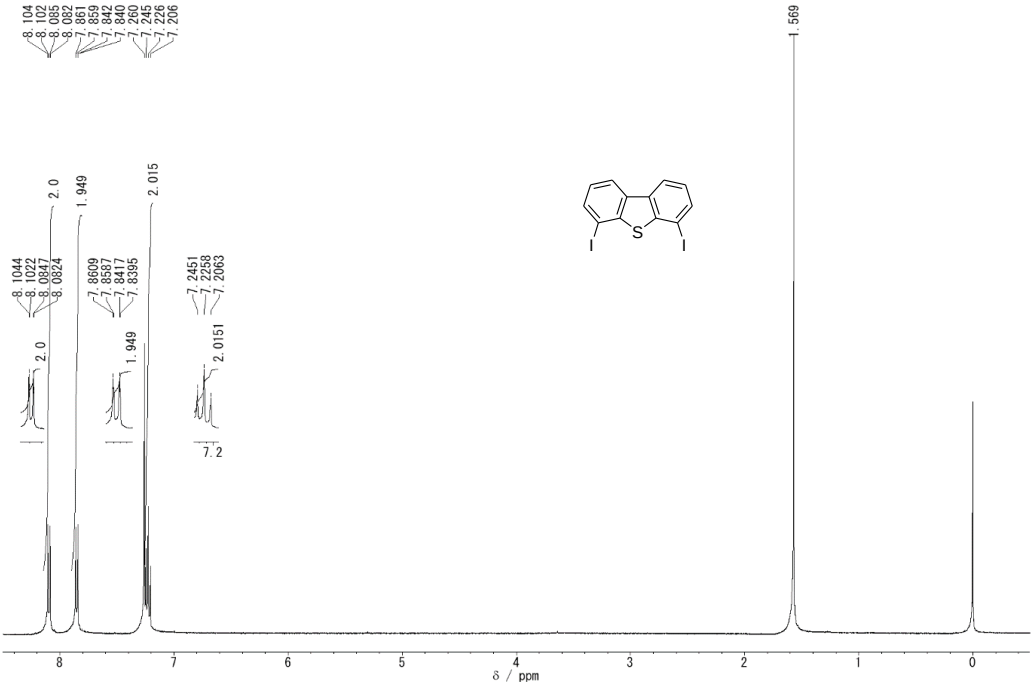

^{1}H NMR spectrum of **2** in $CDCl_3$ solution (400 MHz).

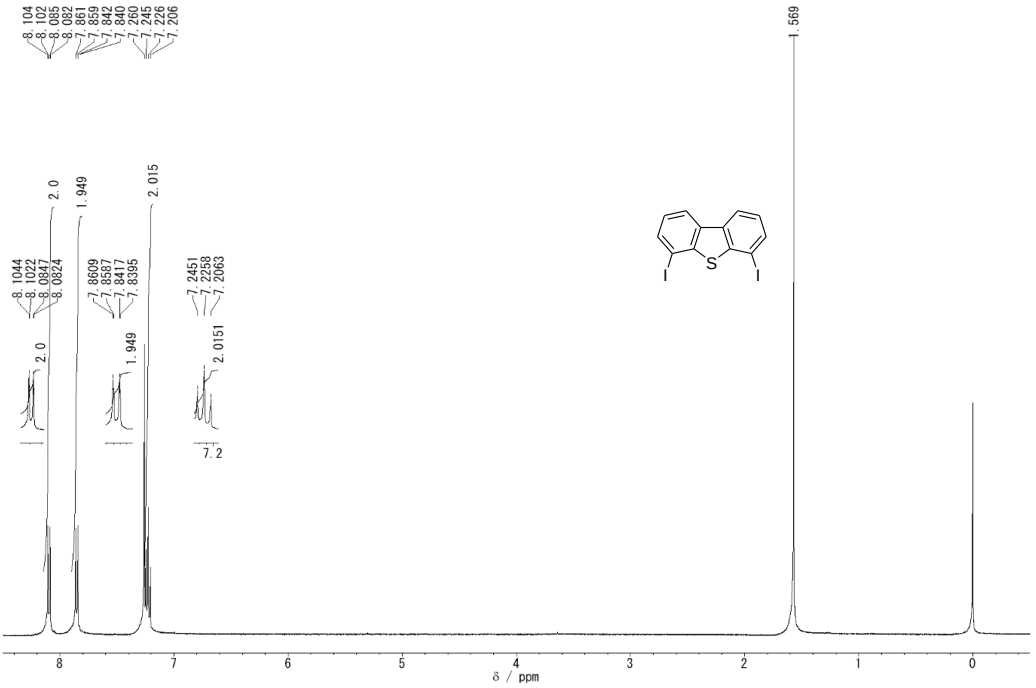

^{13}C NMR spectrum of **2** in $CDCl_3$ solution (100 MHz).

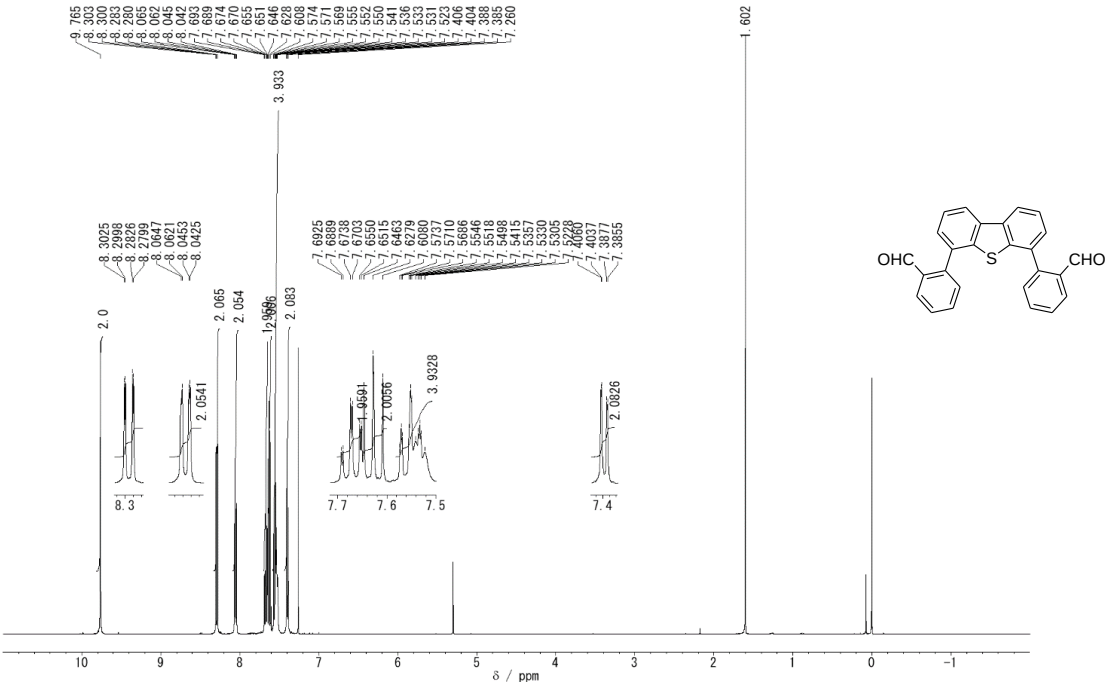

^{1}H NMR spectrum of **4** in $CDCl_3$ solution (400 MHz).

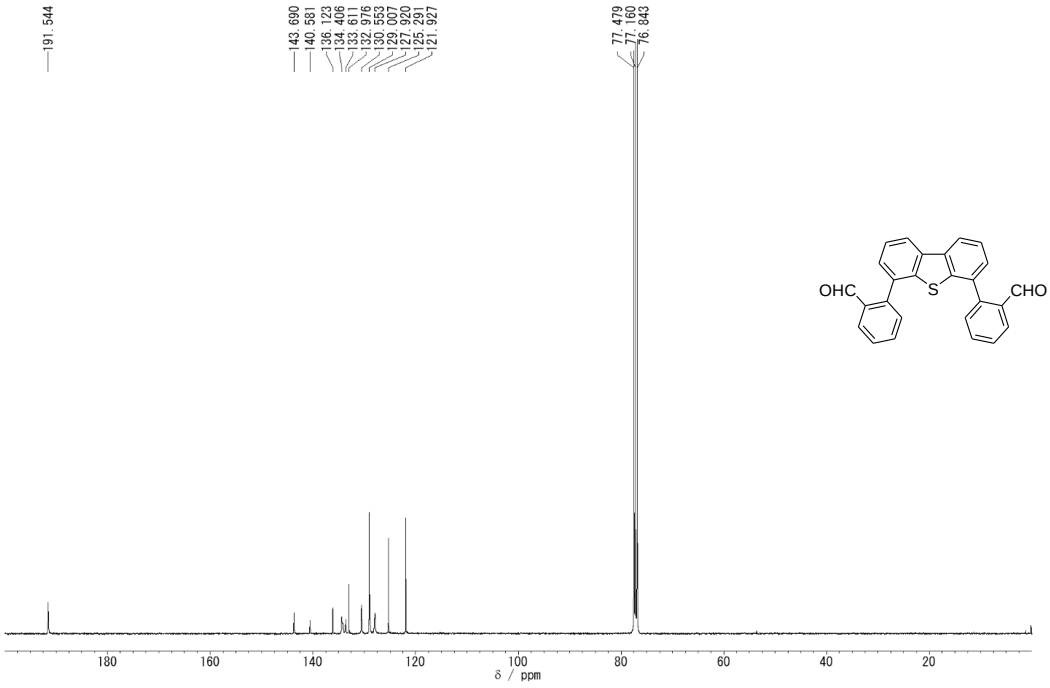

^{13}C NMR spectrum of **4** in $CDCl_3$ solution (100 MHz).

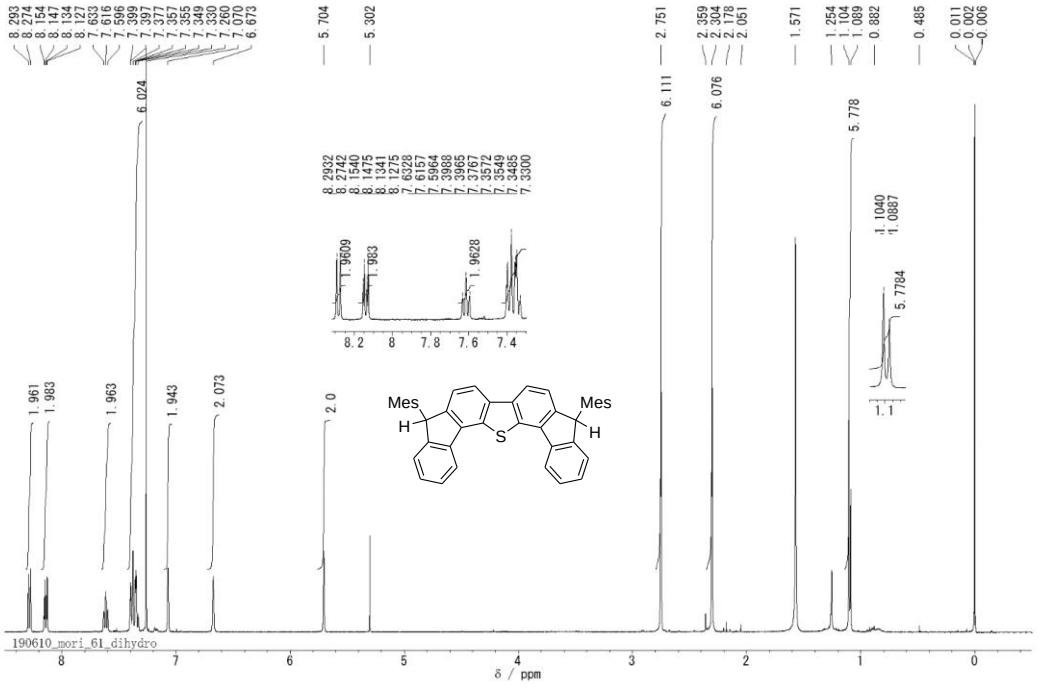

^{1}H NMR spectrum of **6** in $CDCl_3$ solution (400 MHz).

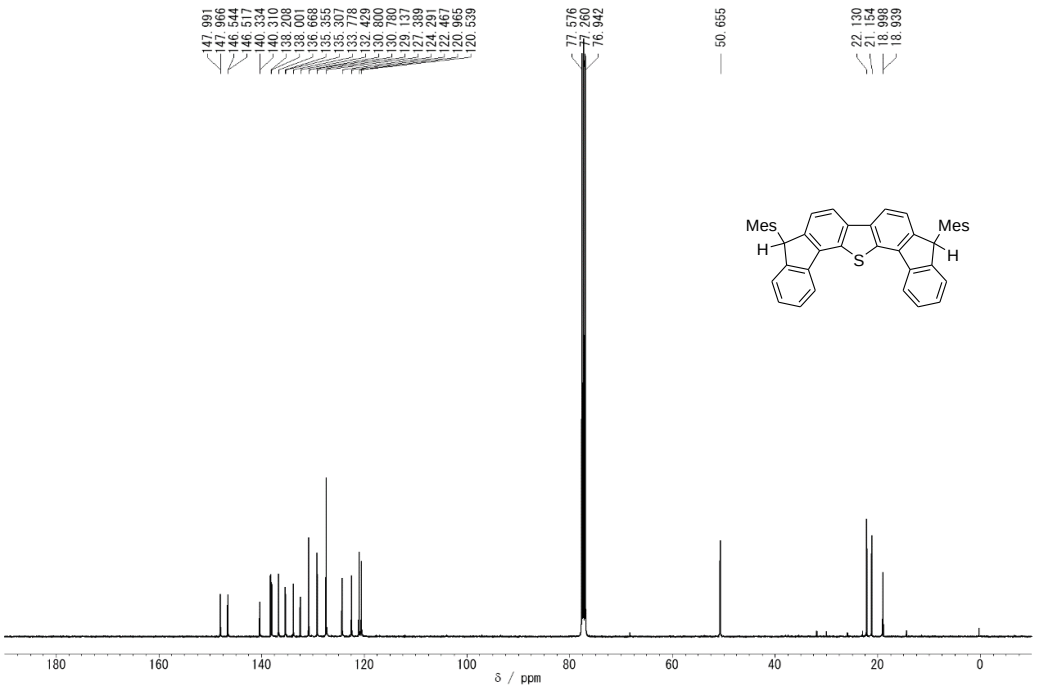

^{13}C NMR spectrum of **6** in $CDCl_3$ solution (100 MHz).

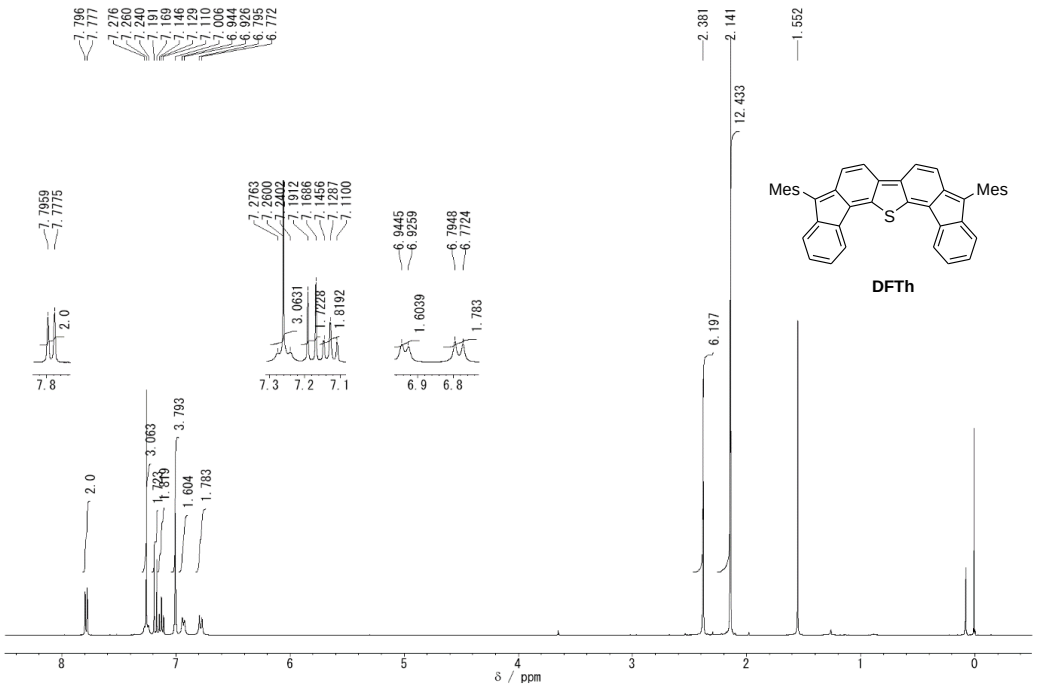

^{1}H NMR spectrum of **DFTh** in $CDCl_3$ solution (400 MHz).

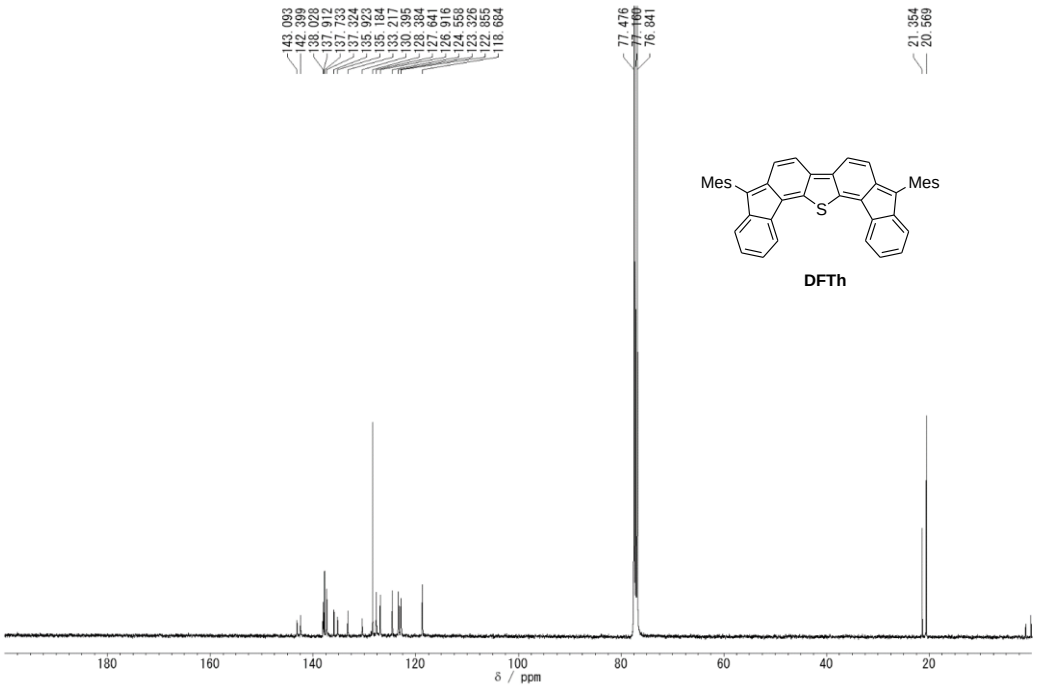

^{13}C NMR spectrum of **DFTh** in $CDCl_3$ solution (100 MHz).

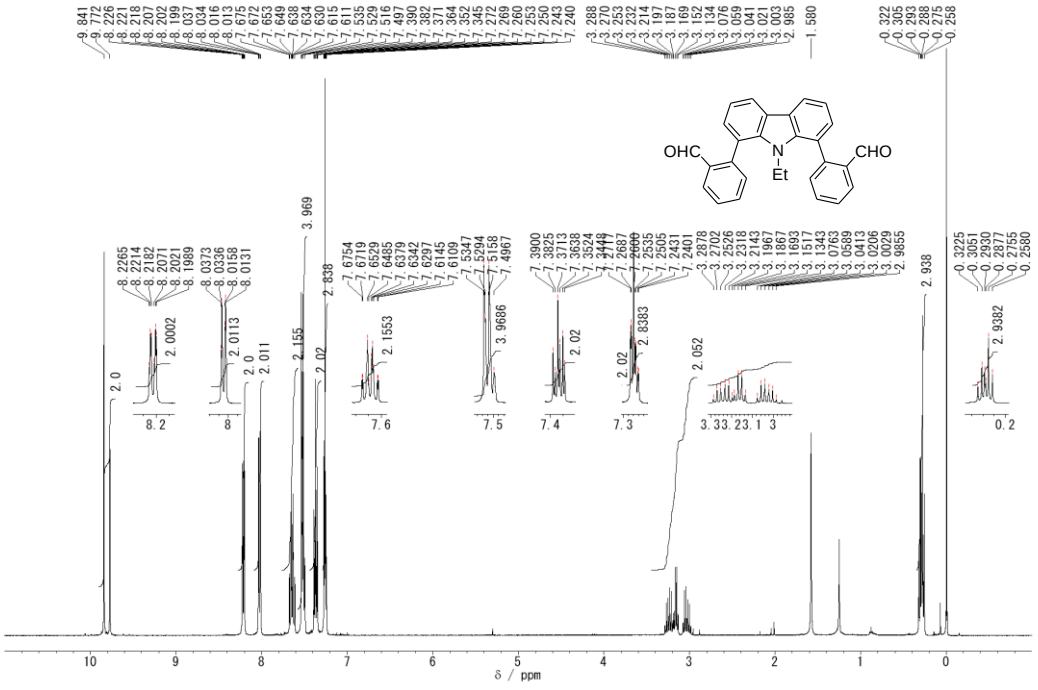

^{1}H NMR spectrum of **5** in $CDCl_3$ solution (400 MHz).

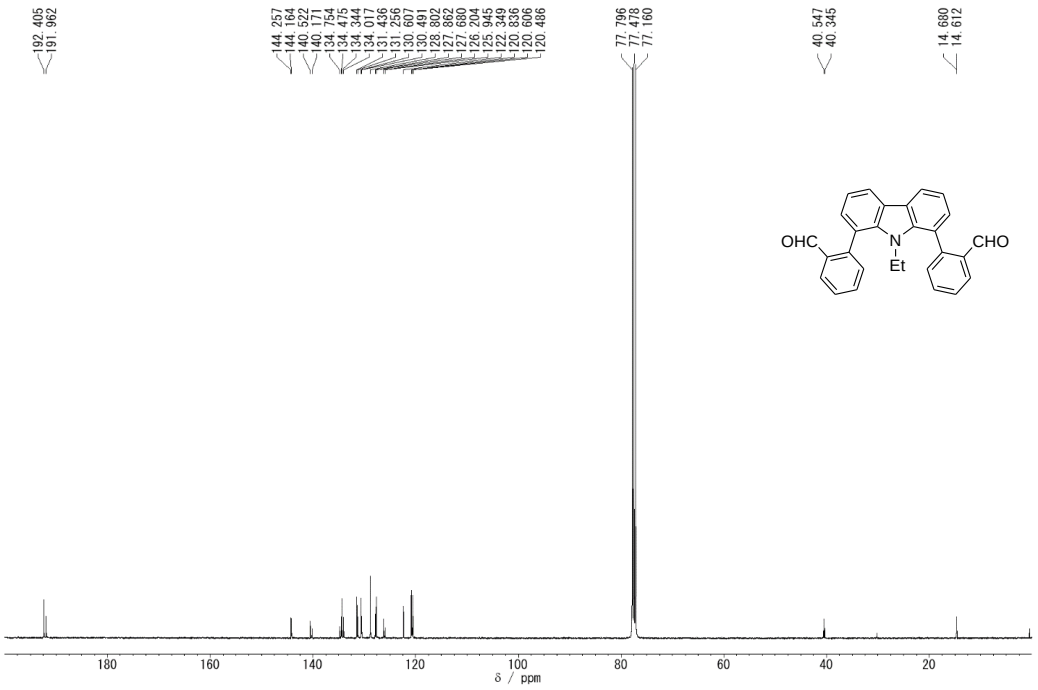

^{13}C NMR spectrum of **5** in $CDCl_3$ solution (100 MHz).

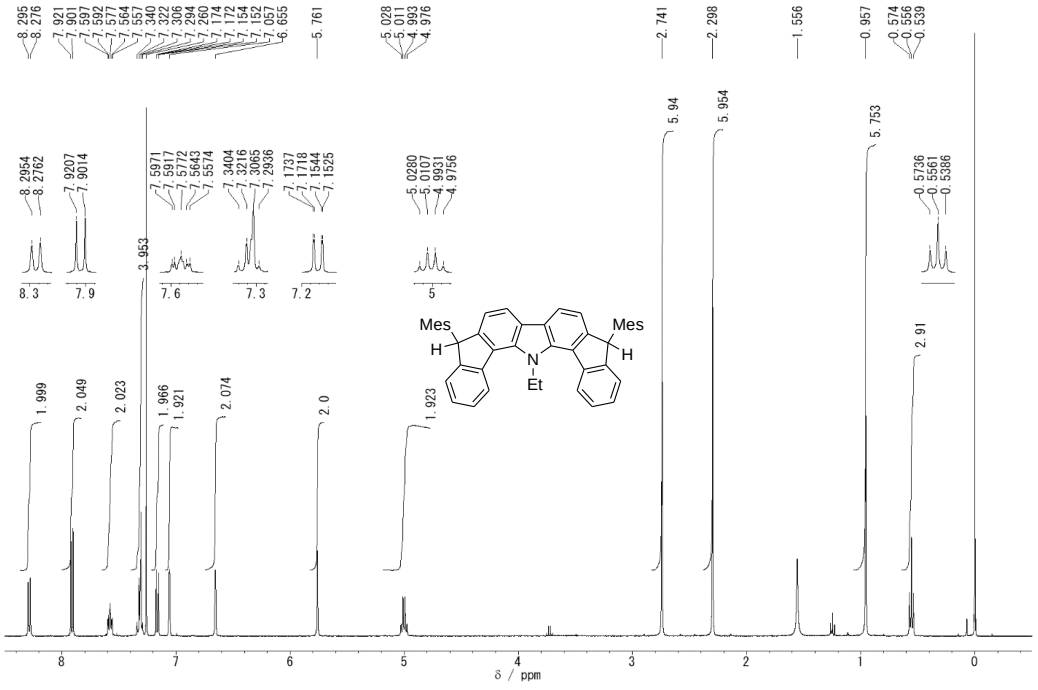

^{1}H NMR spectrum of **7** in $CDCl_3$ solution (400 MHz).

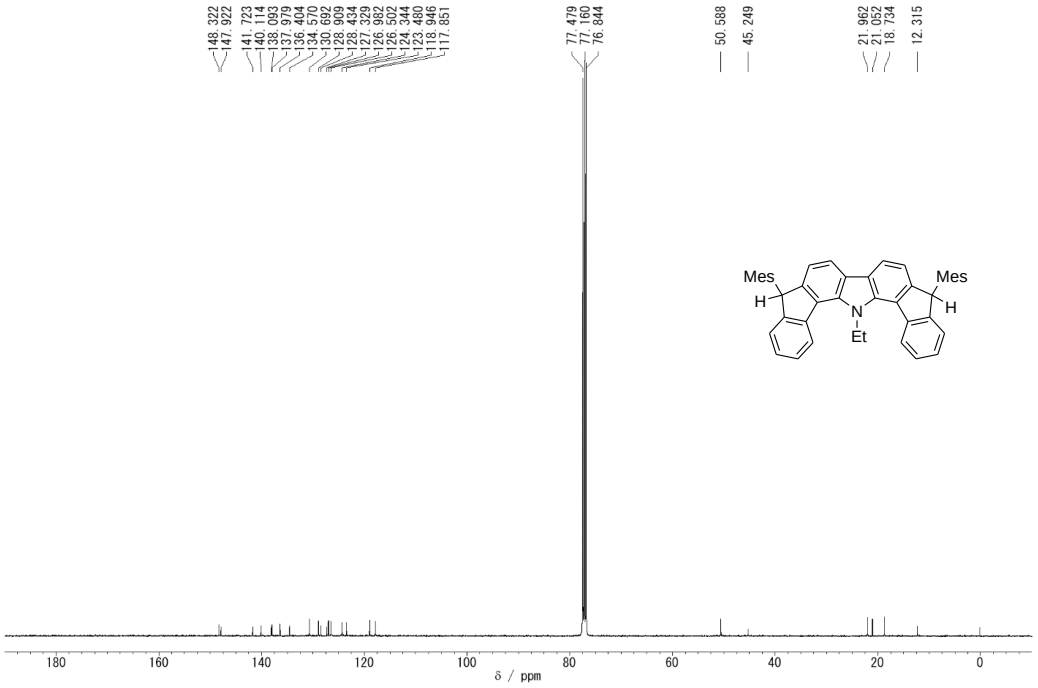

^{13}C NMR spectrum of **7** in $CDCl_3$ solution (100 MHz).

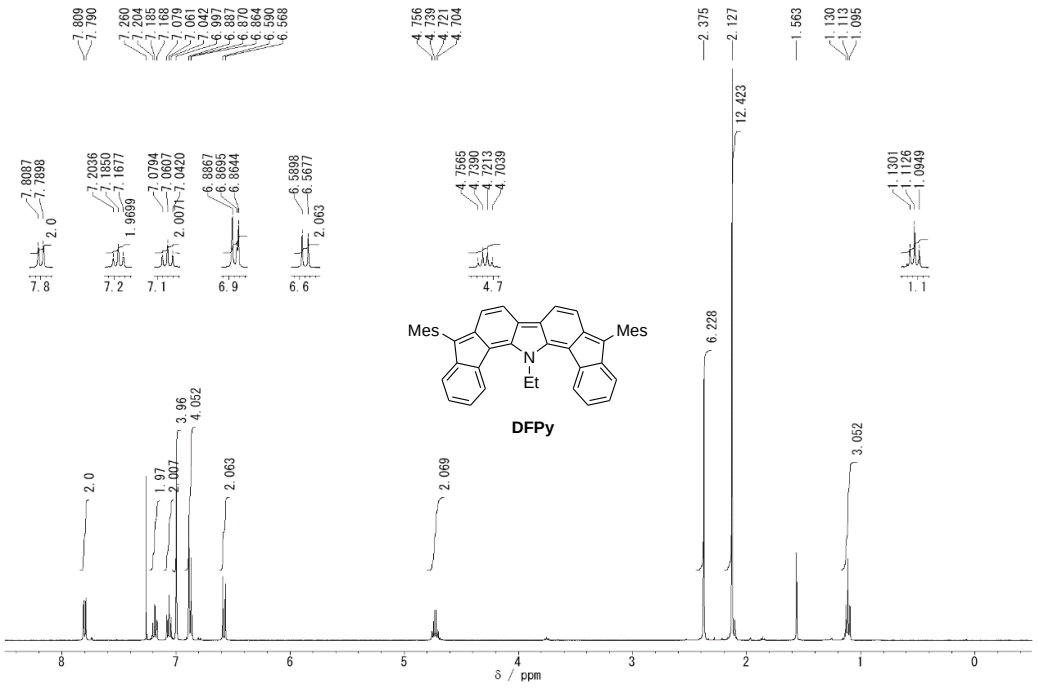

^{1}H NMR spectrum of **DFPy** in $CDCl_3$ solution (400 MHz).

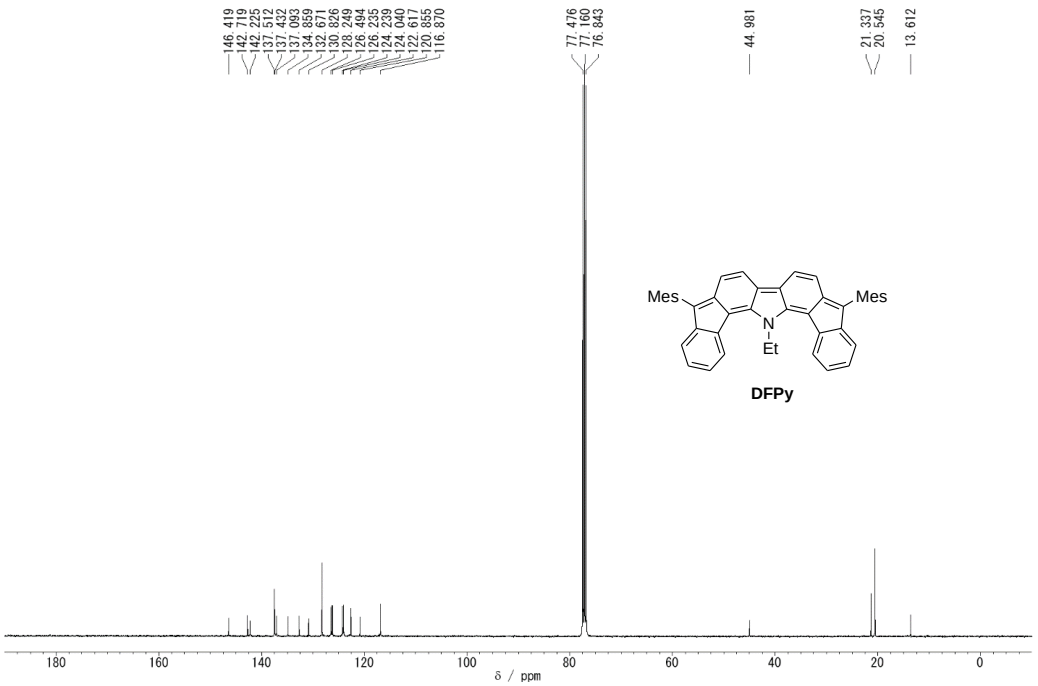

^{13}C NMR spectrum of **DFPy** in $CDCl_3$ solution (100 MHz).

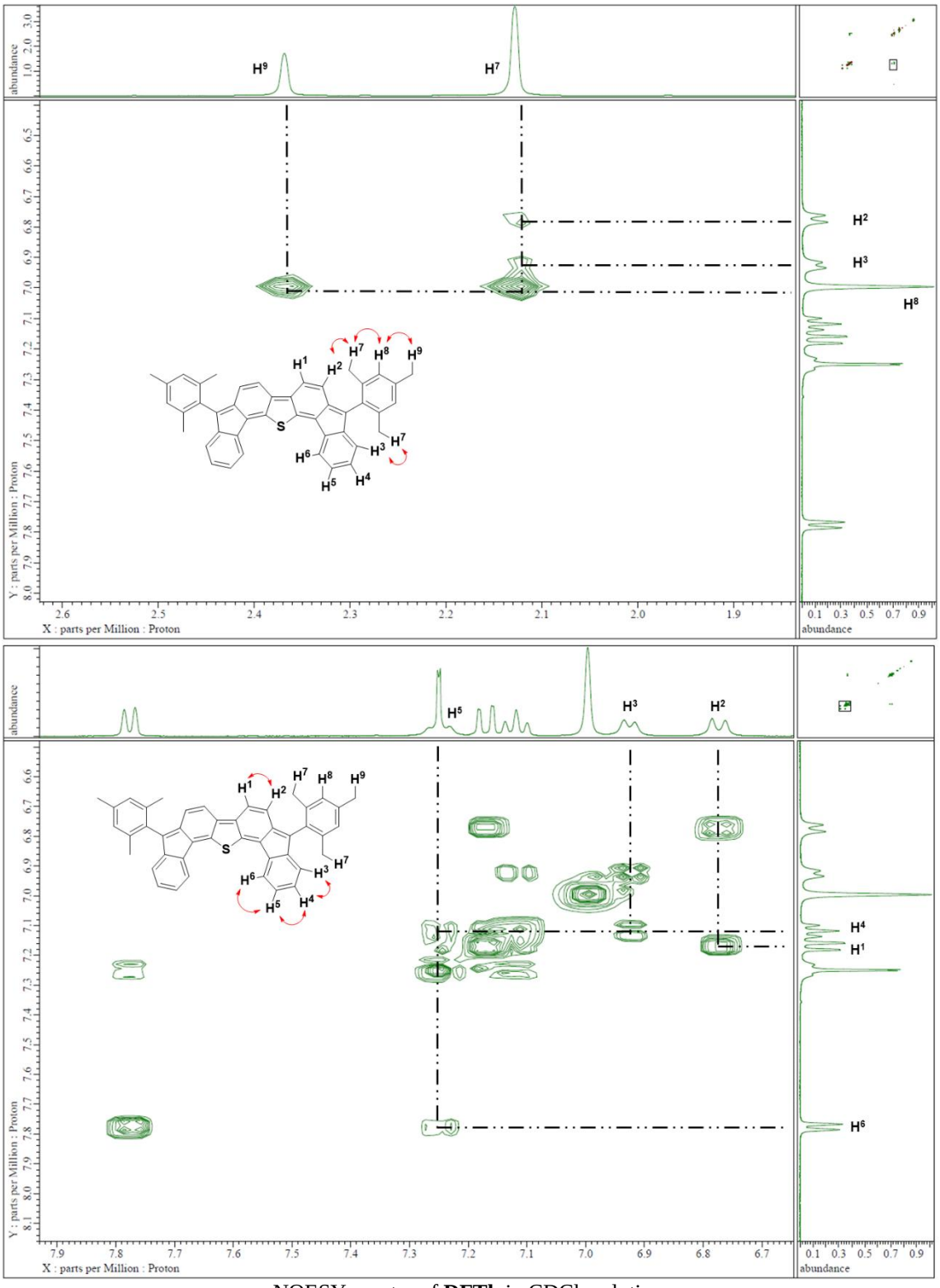

NOESY spectra of **DFTh** in $CDCl_3$ solution.

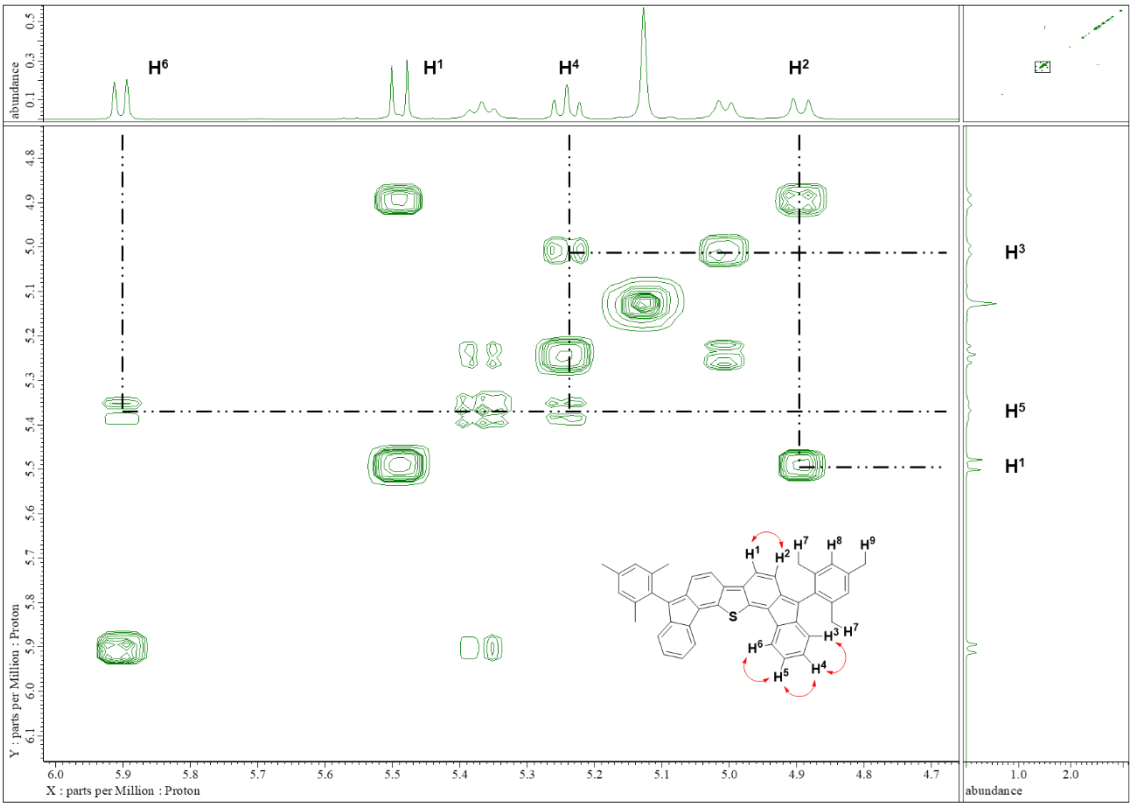

COSY spectrum of **DFTh** in *p*-xylene-d_{10} solution.

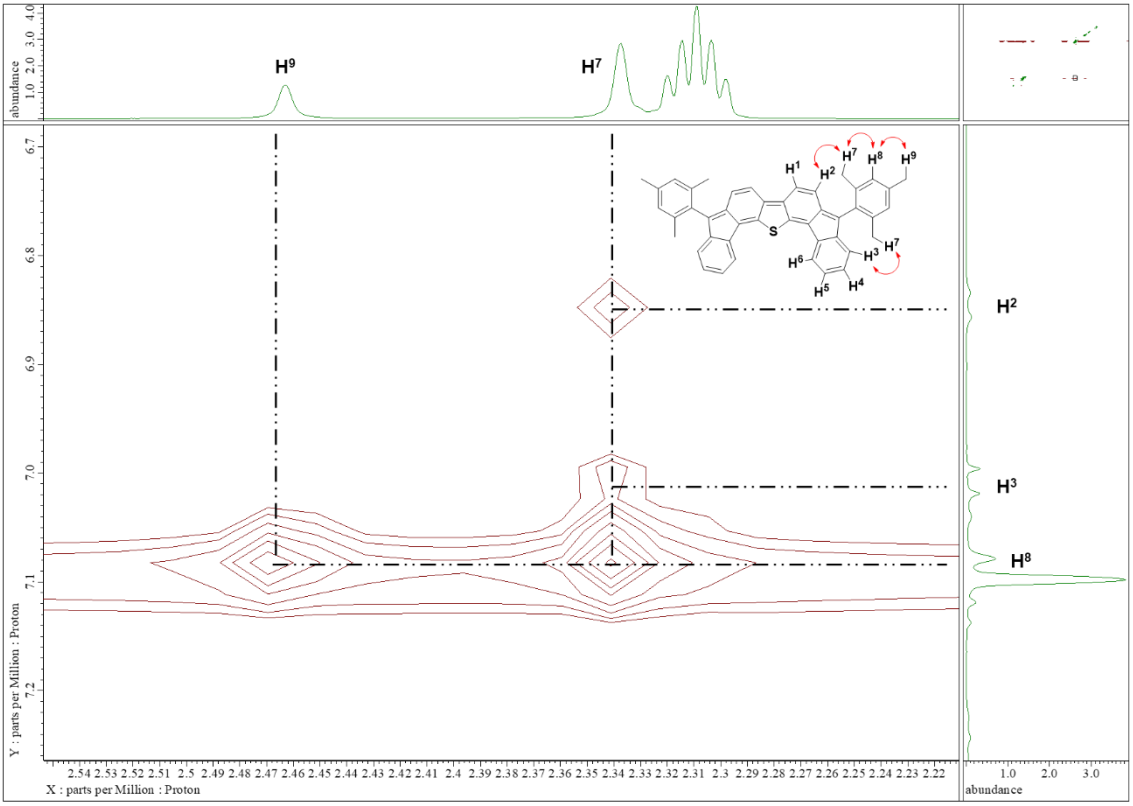

NOESY spectrum of **DFTh** in *p*-xylene-d_{10} solution.

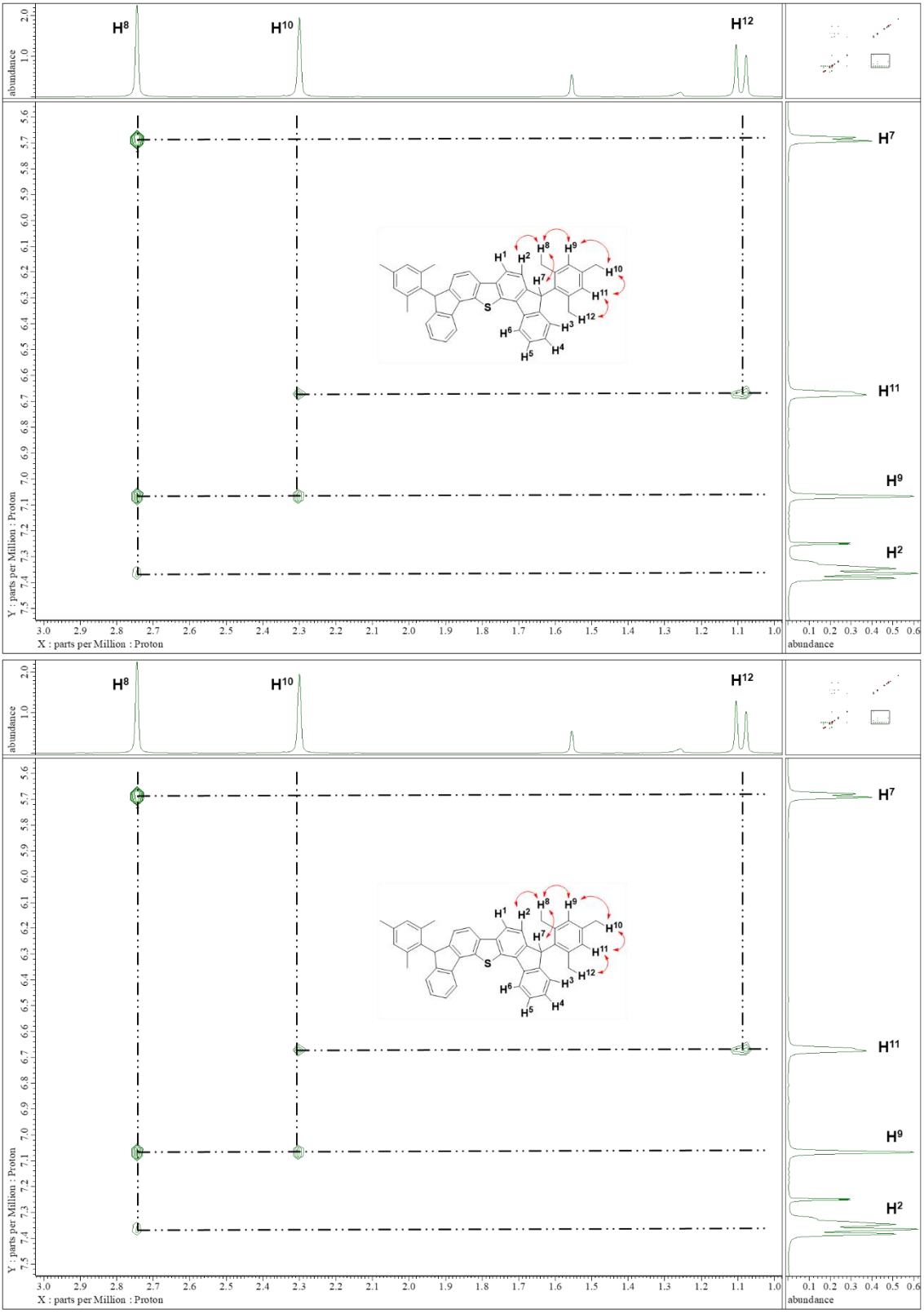

NOESY spectra of dihydro **DFTh** in $CDCl_3$ solution.

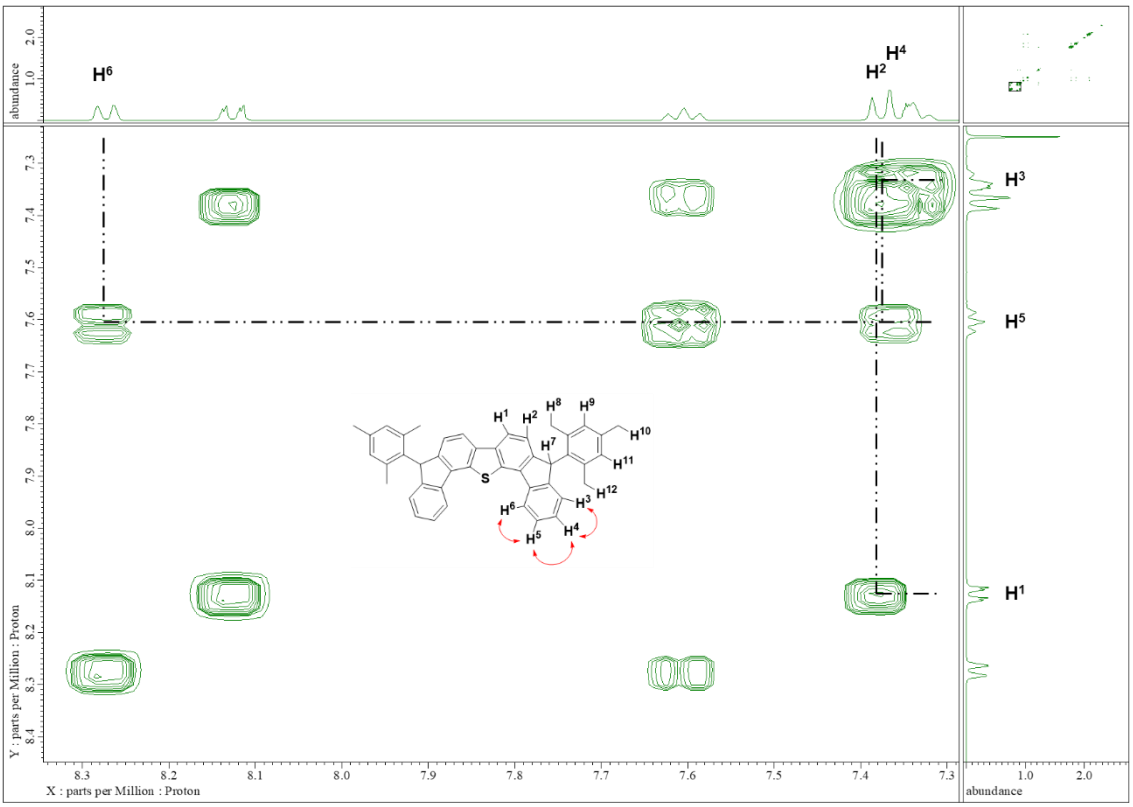

COSY spectrum of dihydro **DFTh** in $CDCl_3$ solution.

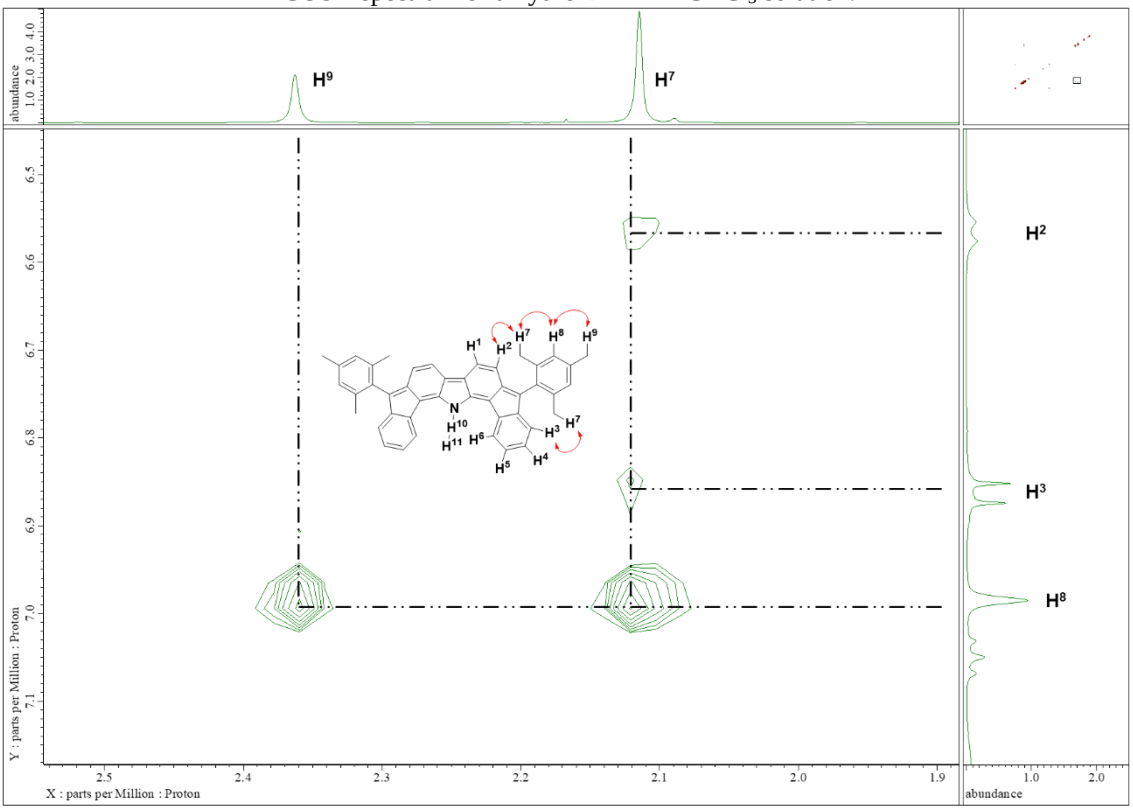

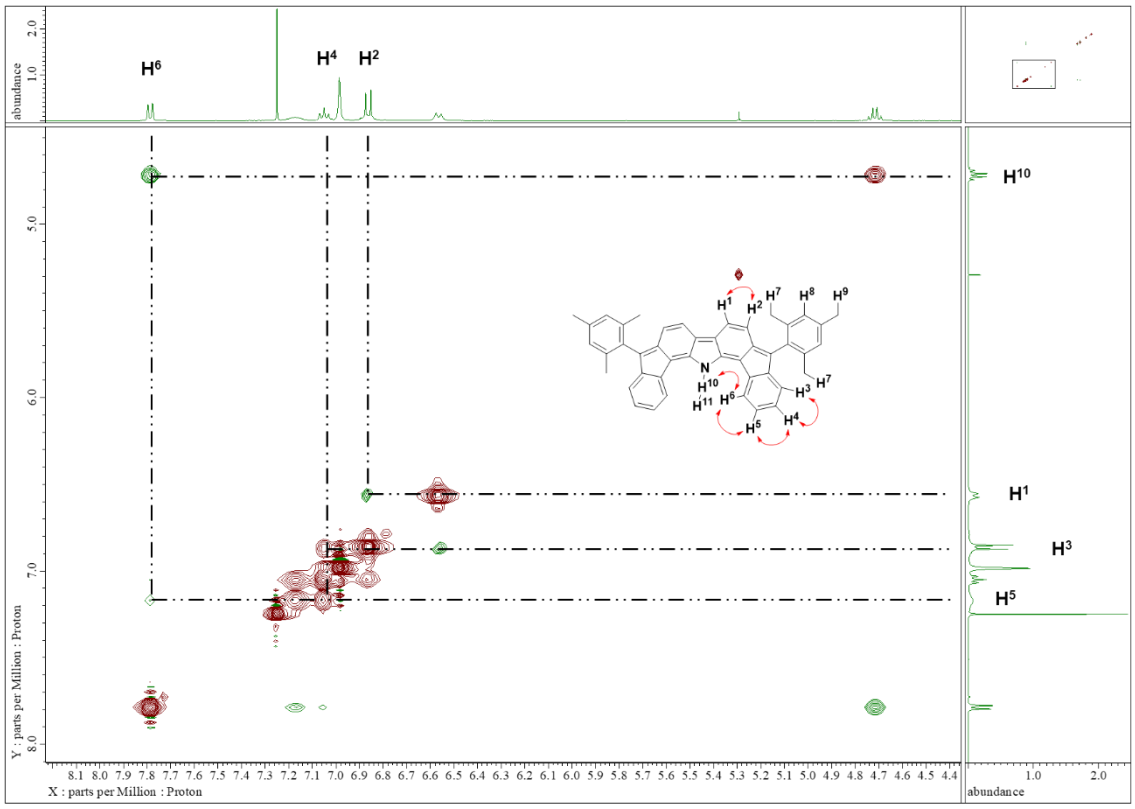

NOESY spectra of **DFPy** in $CDCl_3$ solution.

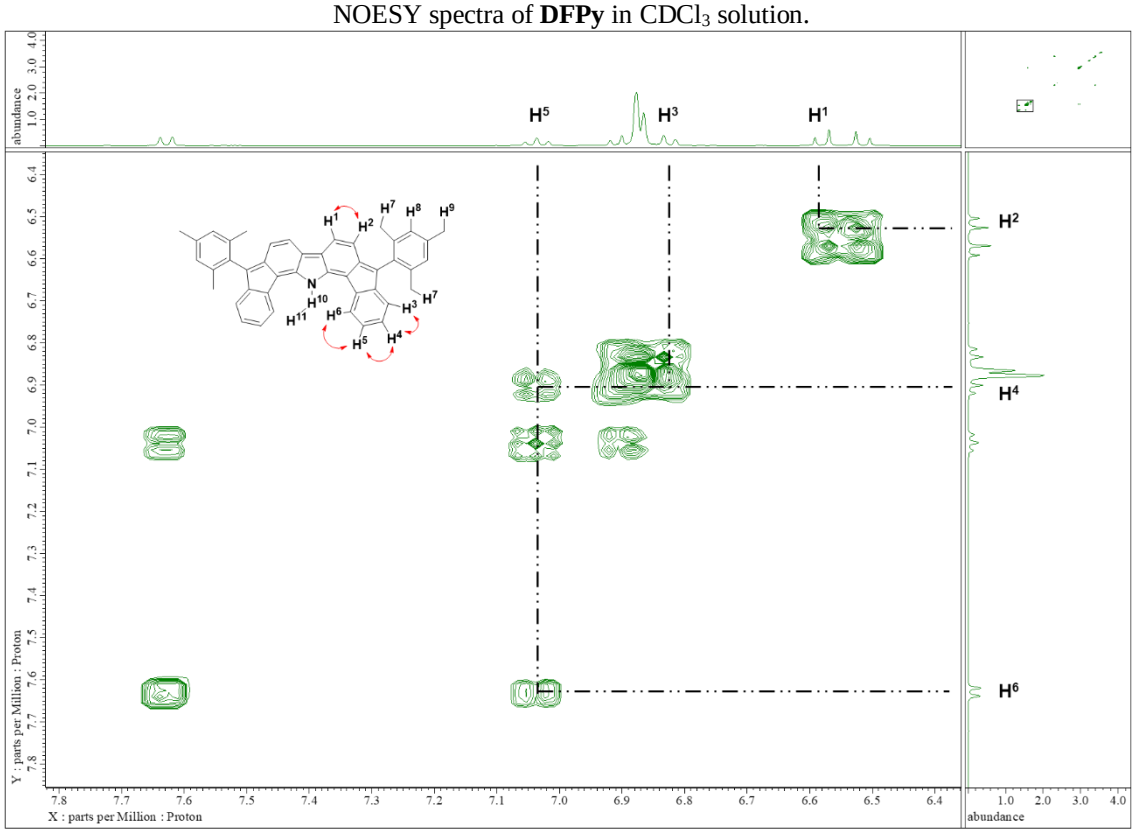

COSY spectrum of **DFPy** in *p*-xylene-d_{10} solution.

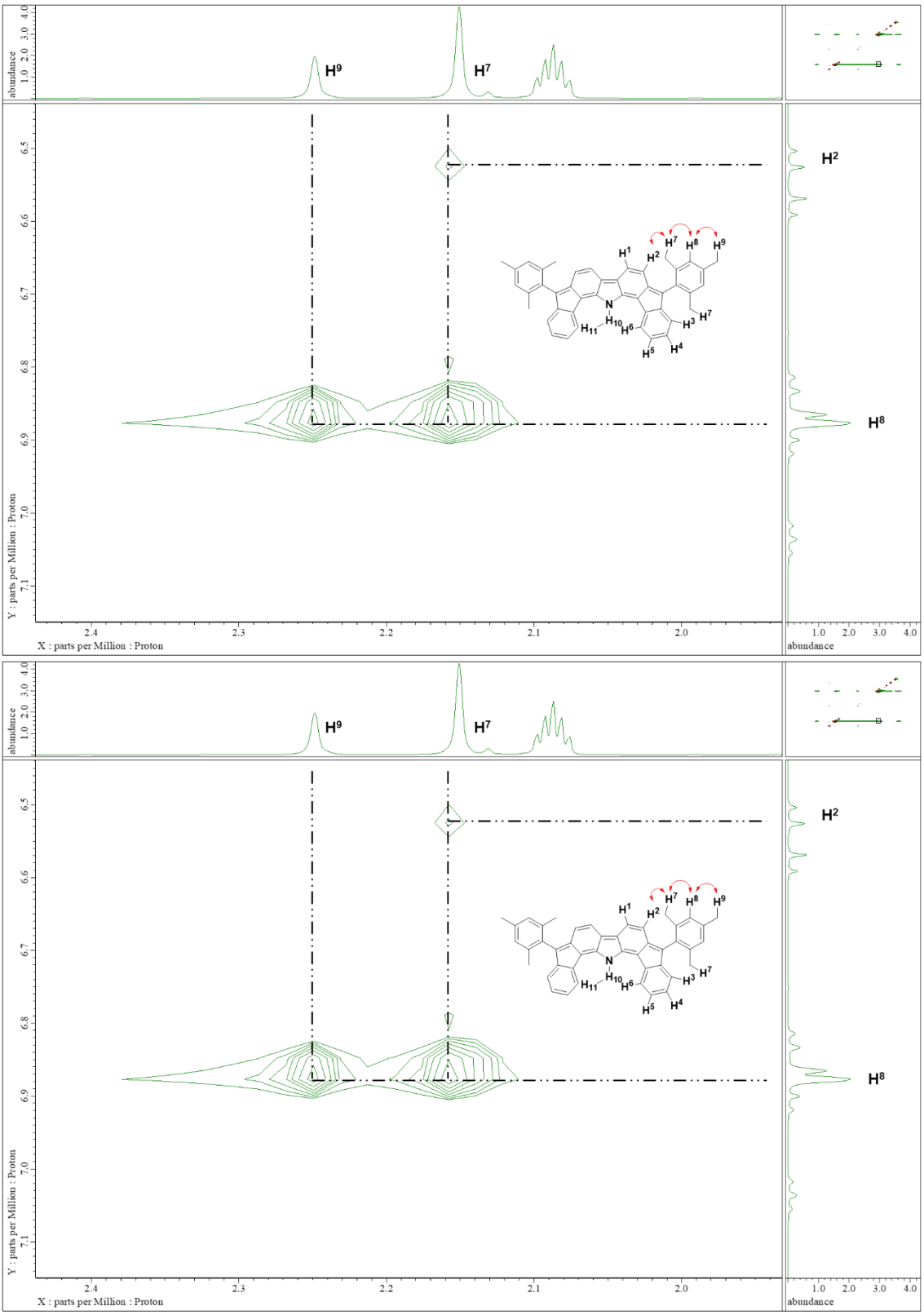

NOESY spectra of **DFPy** in *p*-xylene-d_{10} solution.

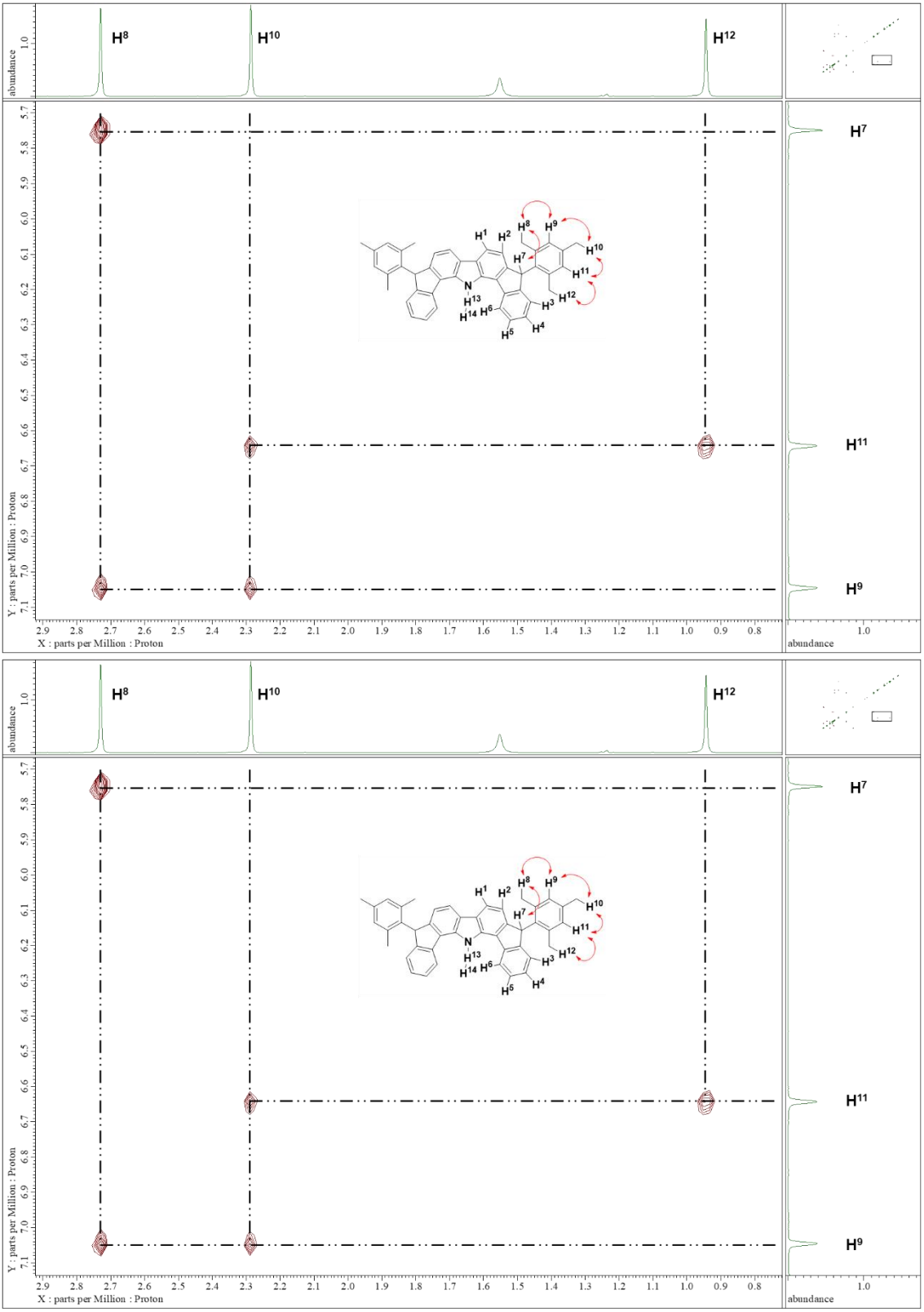

NOESY spectra of dihydro **DFPy** in $CDCl_3$ solution.

X-ray structure details of neutral difluorenoheteroles

General. Low-temperature X-ray diffraction data for **DFTh** and **DFPy** were collected on a Rigaku AFC10 diffractometer coupled to a Rigaku AFC HyPix-6000 detector with Mo Kα radiation (λ = 0.71073 Å) from an FR-E+ X-ray source. The diffraction images were processed and spaced using the CrysAlisPro software.[2] Using Olex2,[3] the structures were solved through intrinsic phasing using SHELXT[4] and refined against F^2 on all data by full-matrix least squares with SHELXL[5] following established refinement strategies. All non-hydrogen atoms were refined anisotropically. All hydrogen atoms bound to carbon were included in the model at geometrically calculated positions and refined using a riding model. The isotropic displacement parameters of all hydrogen atoms were fixed to 1.2 times the Ueq value of the atoms they are linked to (1.5 times for methyl groups). CCDC-1974502 contains the crystallographic data of **DFFu**.

DFTh: crystal data at 123 K, $C_{44}H_{34}S\cdot THF$, M_r = 666.87, monoclinic, space group $P2_1/n$, D_{calcd} = 1.233 g/cm^3, Z = 4, a = 15.4116(6) Å, b = 12.0814(5) Å, c = 19.2966(12) Å, $\alpha = \gamma = 90°$, β = 91.104(4)°, V = 3592.2(3) Å^3; Mo-$K\alpha$ radiation, λ = 0.71073 Å, μ = 0.073 mm^{-1}. A dark green crystal was obtained from THF/MeOH solution at 5 °C. Numbers of measured and unique reflections were 8227 and 5939, respectively. Final $R(F)$ = 0.0494 for 457 parameters and 5939 reflections with $I > 2\sigma(I)$ (for all data, $R(F)$ and $wR(F^2)$ values are 0.0755 and 0.1336, respectively). CCDC-2117204.

DFPy: crystal data at 100 K, $C_{46}H_{39}N\cdot Et_2O$, M_r = 679.90, orthorhombic, space group $Pnma$, D_{calcd} = 1.214 g/cm^3, Z = 4, a = 9.9376(5) Å, b = 35.2667(14) Å, c = 10.6160(4) Å, $\alpha = \beta = \gamma = 90°$, V = 3720.6(3) Å^3; Mo-$K\alpha$ radiation, λ = 0.71073 Å, μ = 0.071 mm^{-1}. A dark green crystal was obtained from Et_2O/MeOH solution at 5 °C. Numbers of measured and unique reflections were 27188 and 4337, respectively. Final $R(F)$ = 0.0513 for 249 parameters and 4337 reflections with $I > 2\sigma(I)$ (for all data, $R(F)$ and $wR(F^2)$ values are 0.0592 and 0.1425, respectively). CCDC-2117205.

DFThO2: crystal data at 113 K, $C_{44}H_{34}O_2S\cdot 0.25$ benzene M_r = 646.30, monoclinic, space group $P2/a$, D_{calcd} = 1.268 g/cm^3, Z = 16, a = 23.7949(11) Å, b = 12.9207(4) Å, c = 44.537(2) Å, $\alpha = \gamma = 90°$, β = 98.646(5)°, V = 13537.1(11) Å^3; Mo-$K\alpha$ radiation, λ = 0.71073 Å, μ = 0.135 mm^{-1}. A dark purple crystal was obtained from benzene/EtOH solution at 5 °C. Numbers of measured and unique reflections were 53846 and 15515, respectively. Final $R(F)$ = 0.0971 for 887 parameters and 15515 reflections with $I > 2\sigma(I)$ (for all data, $R(F)$ and $wR(F^2)$ values are 0.2100 and 0.2696, respectively). CCDC-2165958.

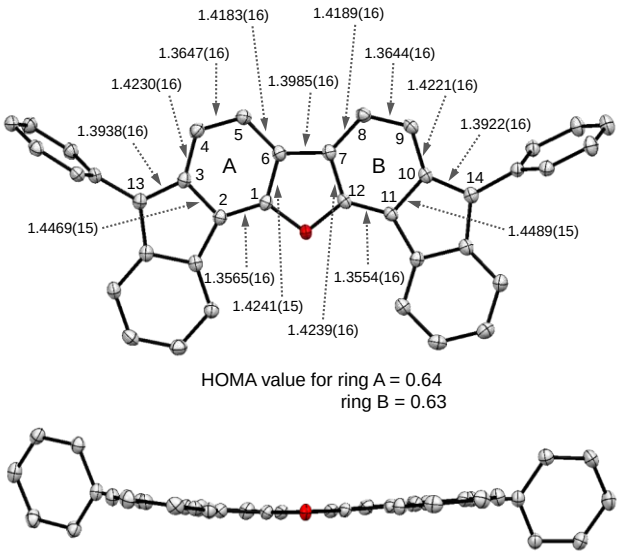

Figure S1. Crystal structure and HOMA of **DFFu** with thermal ellipsoids at 50% probability. Hydrogen atoms and Me groups are omitted for clarity.

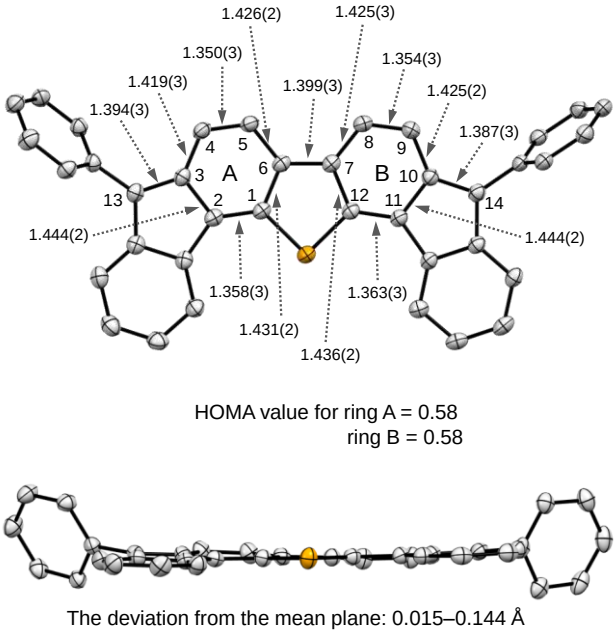

Figure S2. Crystal structure and HOMA of **DFTh** with thermal ellipsoids at 50% probability. Hydrogen atoms and Me groups are omitted for clarity.

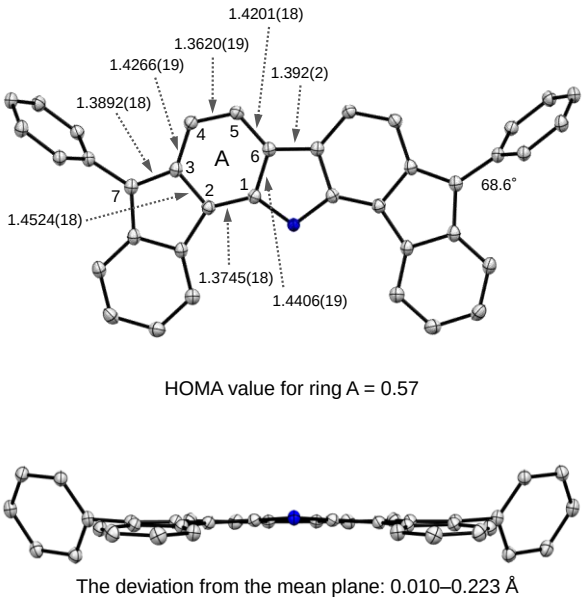

Figure S3. Crystal structure and HOMA of **DFPy** with thermal ellipsoids at 50% probability. Hydrogen atoms and Me and Et groups are omitted for clarity.

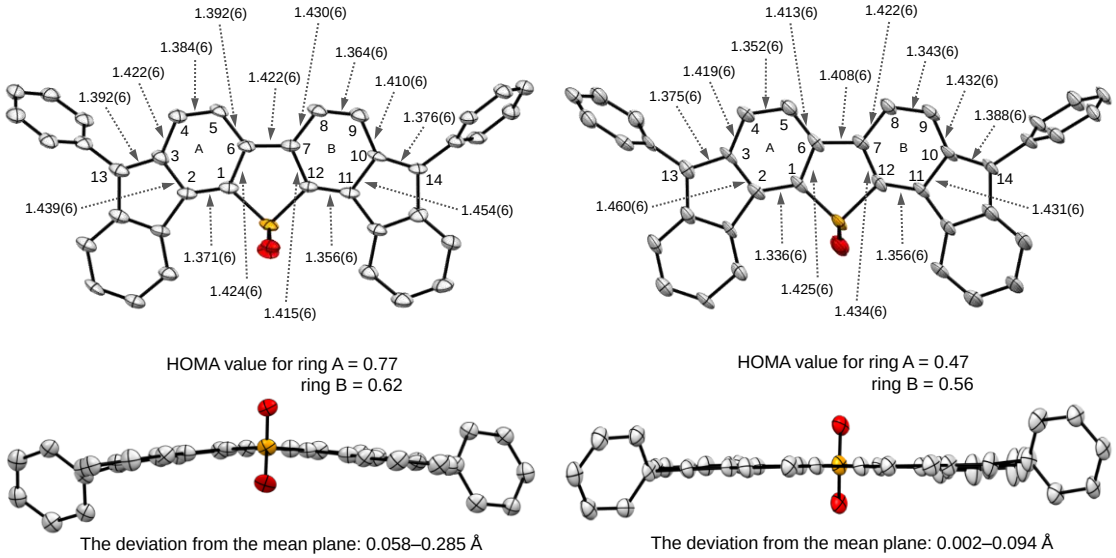

Figure S4. Crystal structure and HOMA of **DFThO2** with thermal ellipsoids at 50% probability. Hydrogen atoms and Me groups are omitted for clarity.

Computational details.

General. We performed gas-phase quantum chemical calculations in order to investigate electronic structures of difluorenoheteroles. Geometry optimization and frequency analysis for **DFFu**, **DFTh** and **DFPy** in the neutral singlet and triplet states were performed at the RB3LYP and UB3LYP levels, respectively, using the 6-311G* basis set. Vertical and adiabatic ΔE_{ST} values were evaluated at the spin-flip noncollinear (SF-NC-)TDDFT PBE50/6-311G* level,[6,7] where zero-point vibrational energy (ZPVE) corrections for the singlet and triplet states were estimated from the results of the frequency analysis calculations at the RB3LYP and UB3LYP levels, respectively. Diradical characters *y* were evaluated at the PUHF/6-311G* level [denoted as *y*(PUHF)].[8] These calculation schemes were reported to reproduce well the experimental geometries and ΔE_{ST} values of several open-shell singlet molecules with intermediate diradical characters.[9]

In order to investigate aromatic characters, we analyzed the nucleous-independent chemical shift (NICS(1))[10] values and the aromaticity of induced current density (ACID) maps.[11] Quality of the results of such magnetic-response-based analysis is sensitive to the choice of calculation method in general. We employed the calculation scheme which was employed in the previous study on di- and tetra-benzofluorenofluorenes.[9] At first, we determined the optimal values of range-separating parameters, μ, in the LC-RBLYP[12] exchange correlation functional. We employed the "IP-tuning" scheme[13] to obtain the optimally tuned values of μ. Then, magnetic responses were evaluated at the GIAO- or CSGT-tuned-LC-UBLYP/6-311G*

Electronic excitation properties of neutrals and radical ions were examined by the TD-tuned-LC-UBLYP/6-311G*. The results of TD-tuned-LC-UBLYP/6-311G* are found to reproduce qualitatively the experimental UV-vis-NIR spectra of neutrals and radical ions. However, the low-lying excited state with double excitation character is in general difficult to be described by the regular TD-DFT. We therefore conducted further excited state calculation of neutral **DFFu** at the *n*-electron valence state perturbation theory (NEVPT2) level.[14] In the NEVPT2 calculation, we at first performed the ground state calculation at the RI-RMP2/6-311G* level where the "AutoAux" scheme[15] implemented in the ORCA package was employed to generate the auxiliary basis set. The RMP2 natural orbitals constructed from the unrelaxed MP2 density were used as the initial orbitals of the state-averaged (SA-)CASSCF(8e,8o)/6-311G* calculation. During the SA-CASSCF calculations, the lowest-lying 10 roots for the singlet state were solved. Then, dynamical correlation effects were taken into account for the diagonal energies at the (RI-)SC-NEVPT2/6-311G* level.

Intramolecular reorganization energy. The intramolecular reorganization energy λ_i was computed with the Adiabatic Potential (AP) method, namely via two-point determinations from each potential energy surface (neutral and charged states) [16]. We determined the closed-shell (CS) and open-shell (OS) broken-symmetry (BS) neutral ground state geometries for all difluoreno-heteroles at RB3LYP and UB3LYP levels of theory, respectively, using the 6-311G* basis set. On the other hand, geometries of the charged states (anion and cation) were determined at UB3LYP/6-311G* level of theory.

Intermolecular electronic coupling. In the framework of the dimer approach and one-electron approximation, the intermolecular electronic coupling ($V_{ij} = \langle \phi_i | \hat{H} | \phi_j \rangle$, where

ϕ_i and ϕ_j are the highest occupied (HOMO) and lowest unoccupied molecular orbitals (LUMO), respectively, of the monomers forming the dimer) can be obtained with a fragment orbital approach. Following previous studies [17], the protocol was based on the determination of the matrix $\boldsymbol{H}_{\mathrm{MOB}}$ in the monomer orbital basis (MOB), whose off-diagonal elements were the non-orthogonalized electronic couplings:

$$\boldsymbol{H}_{MOB} = \boldsymbol{C}^{t}_{MON\_AOB}\boldsymbol{S}_{MON\_AOB}\boldsymbol{C}_{DIM\_AOB}\varepsilon_{DIM}\boldsymbol{C}^{t}_{DIM\_AOB}\boldsymbol{S}_{MON\_AOB}\boldsymbol{C}_{MON\_AOB} \quad (1)$$

where ε_{DIM} is the diagonal matrix of the eigenvalues associated to the molecular orbitals (MO) of the dimer, $\boldsymbol{C}_{DIM\_AOB}$ is the matrix of the eigenvectors of the dimer in the atomic orbital basis (AOB), $\boldsymbol{S}_{MON\_AOB}$ is the overlap matrix of the monomers in the AOB, and $\boldsymbol{C}_{MON\_AOB}$ is the monomer-localized orbitals matrix. $\boldsymbol{C}_{MON\_AOB}$ is, therefore, a block diagonal matrix containing the MO coefficients in the AOB from each monomer, with the off-block diagonals set to zero and the superscript *t* indicating the transpose.
The computed couplings were then transformed in an orthogonalized basis by performing a Löwdin orthogonalization:

$$\boldsymbol{H}^{\perp}_{MOB} = \boldsymbol{S}^{-\frac{1}{2}}_{DIM\_MOB}\boldsymbol{H}_{MOB}\boldsymbol{S}^{-\frac{1}{2}}_{DIM\_MOB} \quad (2)$$

where $\boldsymbol{S}_{DIM\_MOB}$ is the overlap matrix between monomer orbitals, which was obtained as follows from the MO coefficients of the monomer orbitals and the overlap of the atomic orbitals in the dimer configuration $\boldsymbol{S}_{DIM\_MOB}$:

$$\boldsymbol{S}_{DIM\_MOB} = \boldsymbol{C}^{t}_{MON\_AOB}\boldsymbol{S}_{DIM\_AOB}\boldsymbol{C}_{MON\_AOB} \quad (3)$$

For a dimer, this was conducted on the 2 × 2 $\boldsymbol{H}_{MOB}$ matrix including the HOMO (or LUMO) orbitals of the two monomers [18]. A detailed discussion of the approximations involved in the fragment orbital approach was reported in a previous work [19].

The electronic couplings were calculated using B3LYP/6-31G* level of theory at the crystal geometry.

SF-TDDFT and NEVPT2 calculations were performed using Q-Chem 5.3[20] and ORCA 4.2[21] program packages, respectively. All the other quantum chemical calculations were performed using Gaussian 09 rev. D [22] and Gaussian 16 [23].

Table S1. Calculation Results for Diradical Properties of Neutrals.

System	PUHF y_0 [-]	ΔE_{ST} [kcal/mol]		
		Vertical	Adiabatic	Adiabatic (+ZPVE)
DFFu	0.555	–12.45	–6.19	–5.41
DFTh	0.570	–11.61	–5.19	–4.32
DFPy	0.541	–13.22	–6.73	–5.61

Table S2. Optimal Values of μ Determined by IP-tuning Scheme.

System	μ [bohr^{-1}]

DFFu	0.1514
DFTh	0.1490
DFPy	0.1483

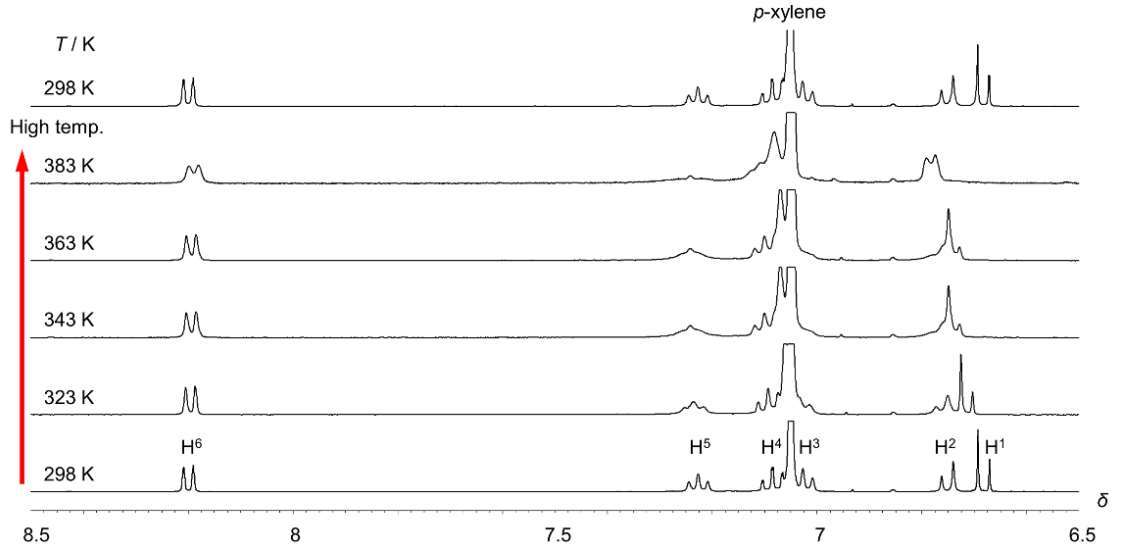

Figure S5. Temperature-dependent ^{1}H NMR spectra of **DFFu** (*p*-xylene-d_{10}, 400 MHz). The original spectrum was fully recovered upon cooling to 298 K. All the signals were fully assigned by 1D NOE and ^{1}H-^{1}H COSY experiments.

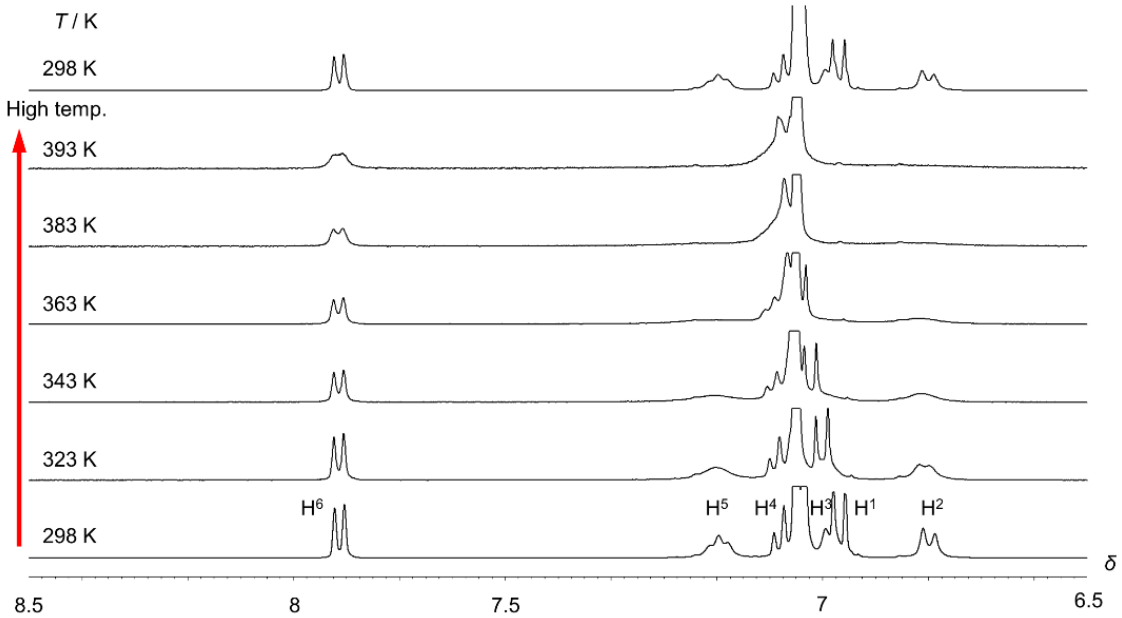

Figure S6. Temperature-dependent ^{1}H NMR spectra of **DFTh** (*p*-xylene-d_{10}, 400 MHz). The original spectrum was fully recovered upon cooling to 298 K. All the signals were fully assigned by 1D NOE and ^{1}H-^{1}H COSY experiments.

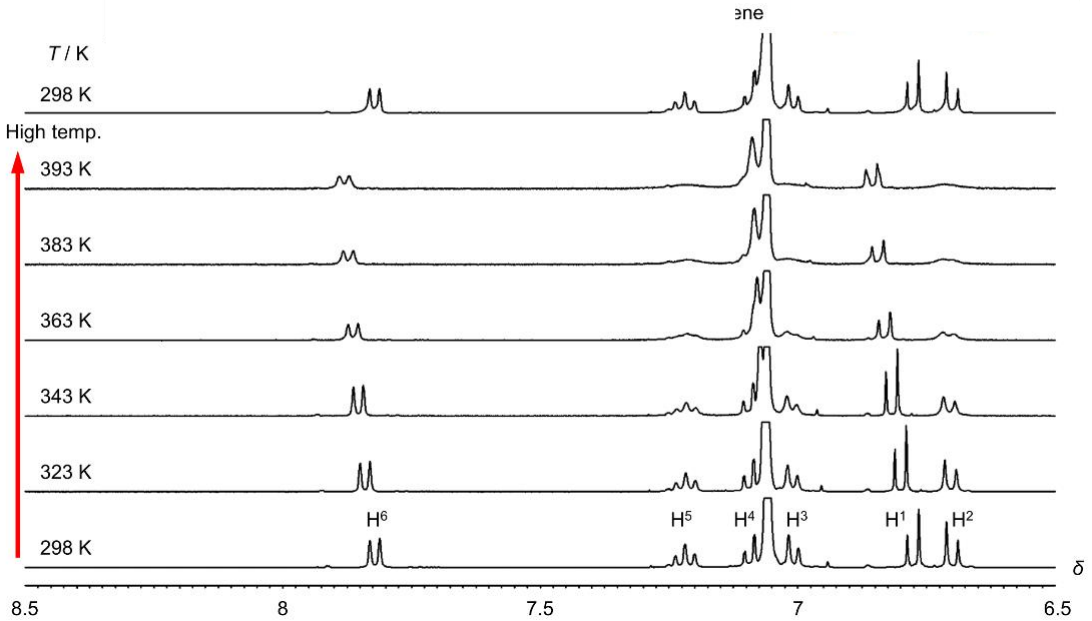

Figure S7. Temperature-dependent ^{1}H NMR spectra of **DFPy** (*p*-xylene-d_{10}, 400 MHz). The original spectrum was fully recovered upon cooling to 298 K. All the signals were fully assigned by 1D NOE and ^{1}H-^{1}H COSY experiments.

Magnetic measurements. Variable temperature susceptibility measurements were carried out with a Quantum Design MPMS-XL-7 SQUID magnetometer, in the temperature range 2-400 K, with an applied magnetic field of 0.5 T, on polycrystalline samples of compounds, sealed in glass capillaries under inert atmosphere. The samples were measured in heating and cooling scans at a scan rate of 2 K/min. The data (and the fits) were very similar in the cooling and heating scans. The susceptibility data were corrected for the empty glass capillary previously measured using the same conditions and for the diamagnetic contribution of the samples as deduced by using Pascal´s constant tables.

Thermal Gravimetric Analysis.

General. Thermogravimetric Analysis (TGA) was performed from 25–450 °C on samples of **DFFu**, **DFTh** and **DFPy** using a Rigaku Thermo Plus TG 8120 instrument. The measurements were performed under an oxygen-free dry N_2 flow.

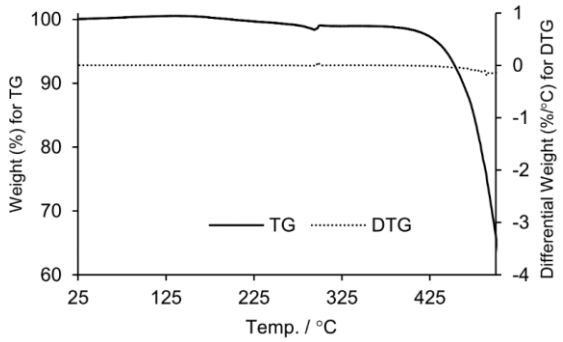

Figure S8. TGA plot for **DFFu**.

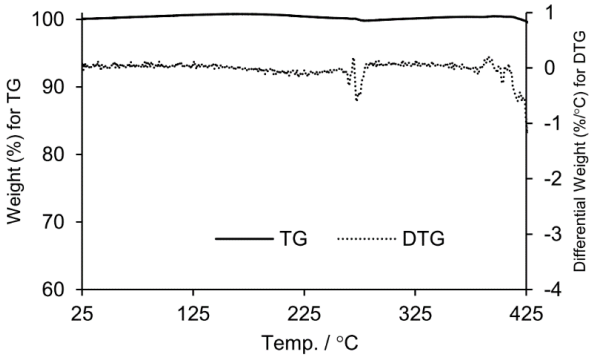

Figure S9. TGA plot for **DFTh**.

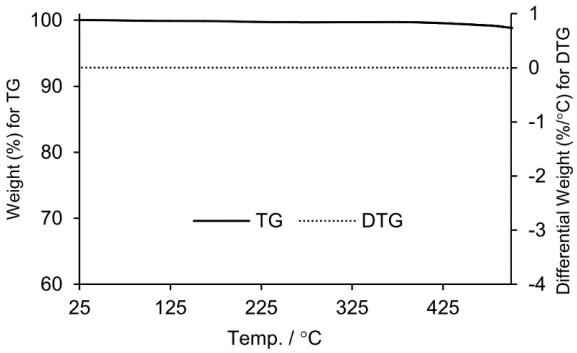

Figure S10. TGA plot for **DFPy**.

Spectroelectrochemical and cyclic voltammetry experiments.

Cyclic voltammetry experiments: Cyclic voltammetry (EC Frontier ECstat-100) was performed using a cell equipped with a platinum wire working electrode, a platinum wire counter electrode, and an $Ag/AgNO_3$ reference electrode. All electrochemical measurements were performed in CH_2Cl_2 solution (ca. 0.5 mM) containing 0.1 M $[(n\text{-}Bu)_4N][PF_6]$ at room temperature. All potentials are referenced to the ferrocenium/ferrocene (Fc^+/Fc) couple, which was used as a standard.

Table S3. Redox Potentials and Comproportionation Constants K_c^{RC} and K_c^{RA}

Cmpd.	CV [a]		DPV [b]		ΔE_{redox} [V] [c]	K_c^{RC}	K_c^{RA}
	E_{ox} [V]	E_{red} [V]	E_{pa} [V]	E_{pc} [V]			
DFFu	+0.32	−1.17	+0.30	−1.16	1.49	1.7×10^8	5.2×10^5

DFTh	+0.81	−1.51	+0.78	−1.52	1.45	3.6×10^7	3.5×10^5
	+0.31	−1.14	+0.32	−1.10			
	+0.76	−1.47	+0.78	−1.44			
DFPy	+0.17	−1.31	+0.14	−1.28	1.48	1.2×10^9	7.6×10^5
	+0.71	−1.66	+0.70	−1.64			

[a] Scan rate 100 mV s^{-1}. [2] 0.1 sec in period of 0.2 sec. [c] $\Delta E_{redox} = E^1_{ox} - E^1_{red}$.

Table S4. HOMO and LUMO energies of the four difluorenoheterole derivatives calculated at optimized BS and CS geometries using UB3LYP and RB3LYP functionals, respectively. 6-311G* basis set is used.

	Neutral (BS)		**Neutral (CS)**	
Compound	H / eV	L / eV	H / eV	L / eV
DFPy	-4.88	-3.07	-4.79	-3.19
DFFu	-5.04	-3.18	-4.91	-3.34
DFTh	-5.06	-3.20	-4.91	-3.38
DFThSO$_2$	-5.29	-3.41	-5.12	-3.63

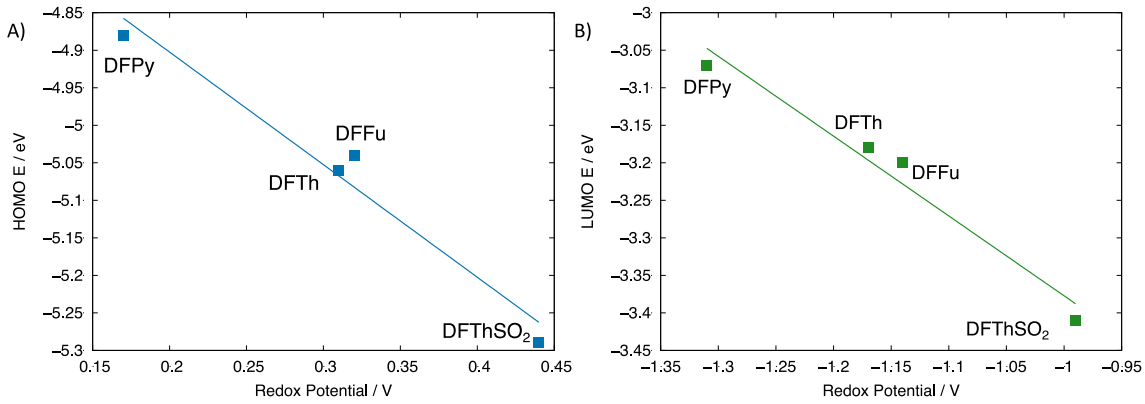

Figure S11. Correlation between experimental redox potentials and computed MO energies of the four molecules. A) correlation between the first oxidation potential (from cyclic voltammetry, Table 1 and Table S3) and the HOMO energies (Table S4); B) correlation between the first reduction potential (from cyclic voltammetry, Table 1 and Table S3) and the LUMO energies (Table S4). MO energies calculated at UB3LYP/6-311G* level of theory.

Spectroelectrochemical experiments: Electrochemical experiments have been conducted in CH_2Cl_2 at room temperature by using 0.1 M tetrabutyl ammonium hexafluorophosphate, [(*n*-Bu)$_4$N][PF_6], as the supporting electrolyte. In situ UV-Vis-NIR spectroelectrochemical studies were conducted on the Varian Cary 5000 UV-Vis-NIR Spectrophotometer, respectively. A C3 epsilon potentiostat from BASi was used for the electrolysis using a thin layer cell from a demountable omni cell from Specac. In this cell a three electrodes system was coupled to conduct in situ spectroelectrochemistry. A Pt gauze was used as the working electrode, a Pt wire was used as the counter electrode, and an Ag wire was used as the pseudo-reference electrode. The spectra were collected a constant potential electrolysis and the potentials were changed in interval of 15 mV. The electrochemical medium used was 0.1 M [(*n*-Bu)$_4$N][PF_6] in fresh distilled CH_2Cl_2, at room temperature with sample concentrations of 10^{-3} M.

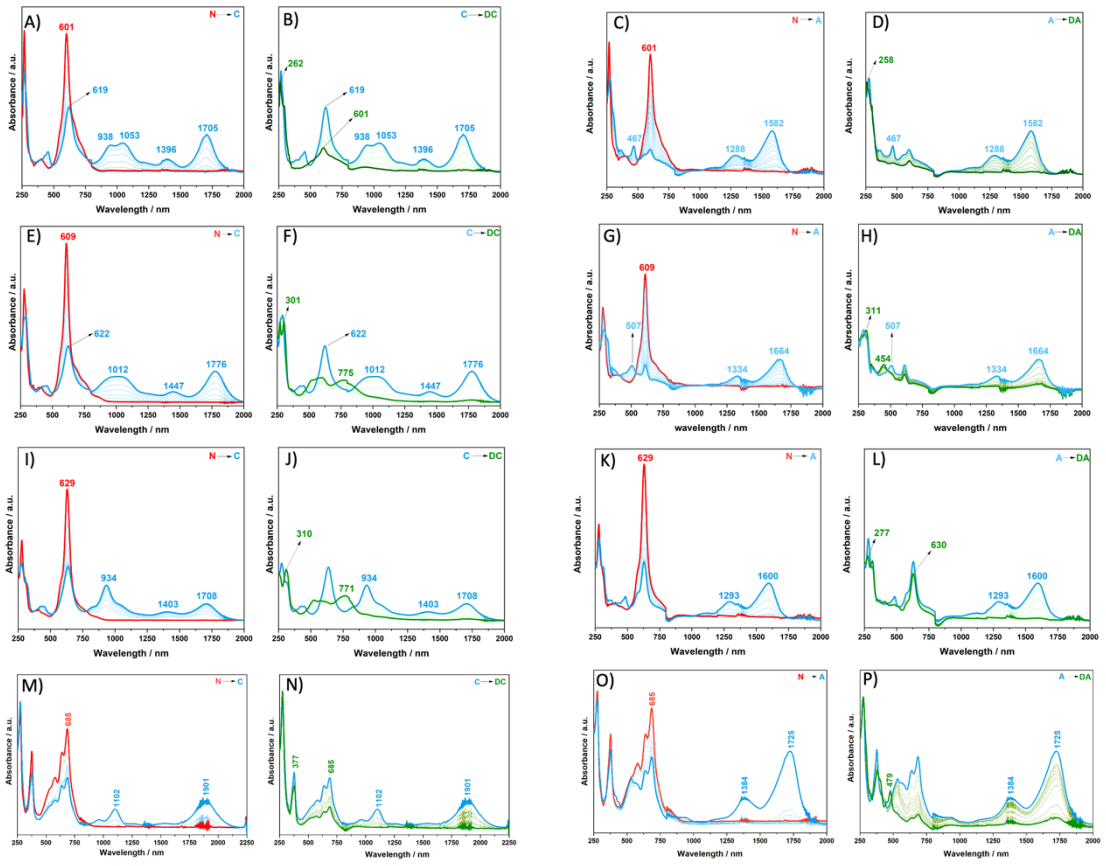

Figure S12. UV-Vis-NIR spectroelectrochemical reduction in 0.1 M [(*n*-Bu)$_4$N][PF_6] in CH_2Cl_2 at room temperature. From the top: **DFFu** (A-D), **DFTh** (E-H), **DFPy** (I-L) and **DFThO$_2$** (M-P). Right: transformation from neutral to radical cation (A,E,I,M), from radical cation to dication (B,G,J,O), from neutral to radical anion (C,G,K,O) and from radical anion to dianion (D,H,L,P). reduction process. Red lines correspond to the spectra of neutral species, blue lines correspond to the anionic/cationic species. Green lines correspond to dication/dianion.

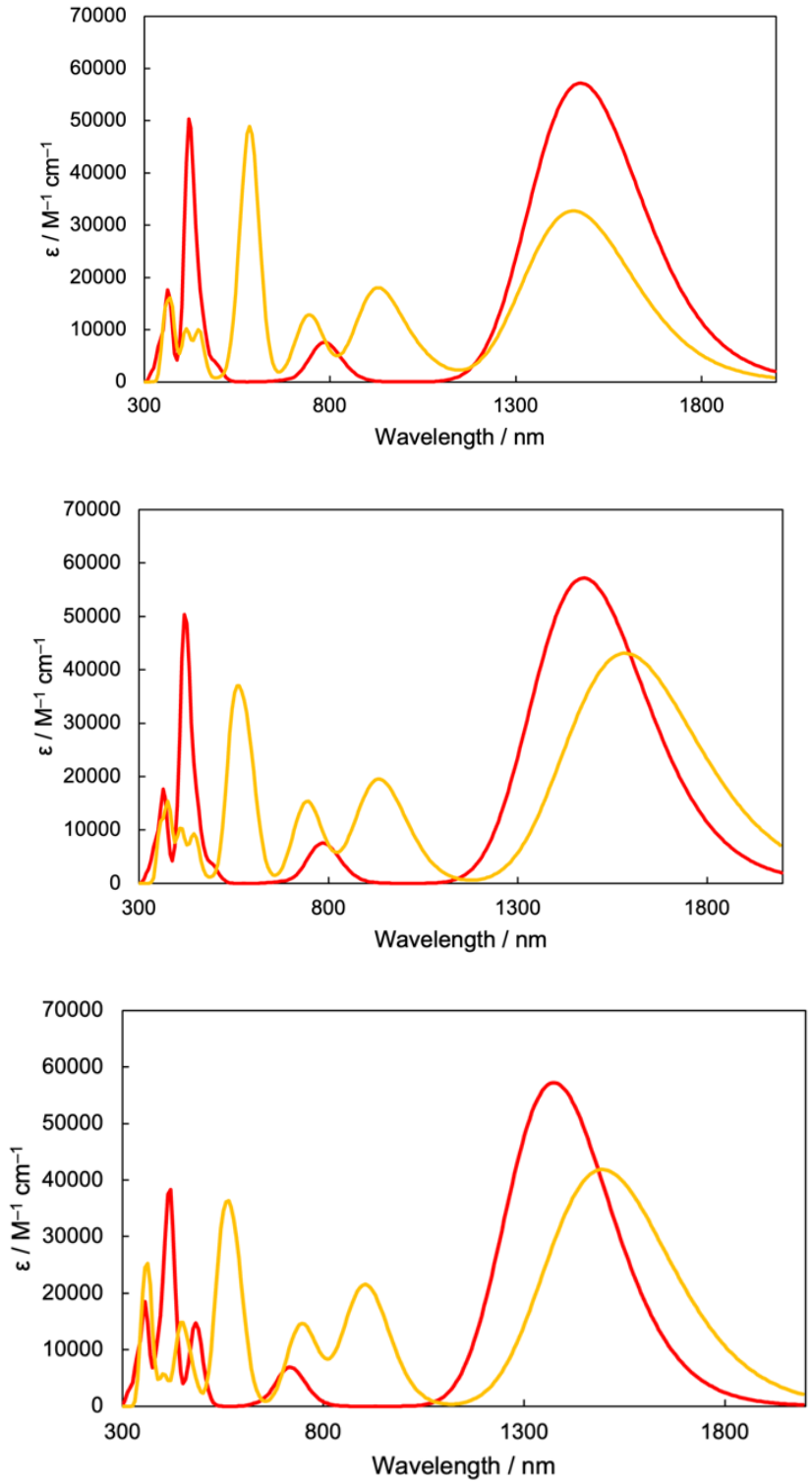

Figure S13. TD-DFT results for UV-vis-NIR spectra of radical anions (red) and cations (yellow). From the bottom: **DFFu**, **DFTh** and **DFPy**.

Photophysics properties. Transient absorption study.

Femtosecond transient absorption spectroscopy characterization was carried out with a Helios equipment from Ultrafast Systems, equipped with an amplified femtosecond Spectra-Physics Solstice-100F laser (with a 128 fs pulse width and 1 KHz repetition rate) coupled with a Spectra-Physics TOPAS Prime F optical parametric amplifier (195-22000 nm). Samples were studied in a 20 µM solution in CH_2Cl_2, with an excitation wavelength of 600, 630 and 610 nm for **DFFu**, **DFPy** and **DFTh**, respectively. The excitation power was modified using neutral density filters to match the desired power (0.06, 0.125, 0.25 and 0.5 mW).

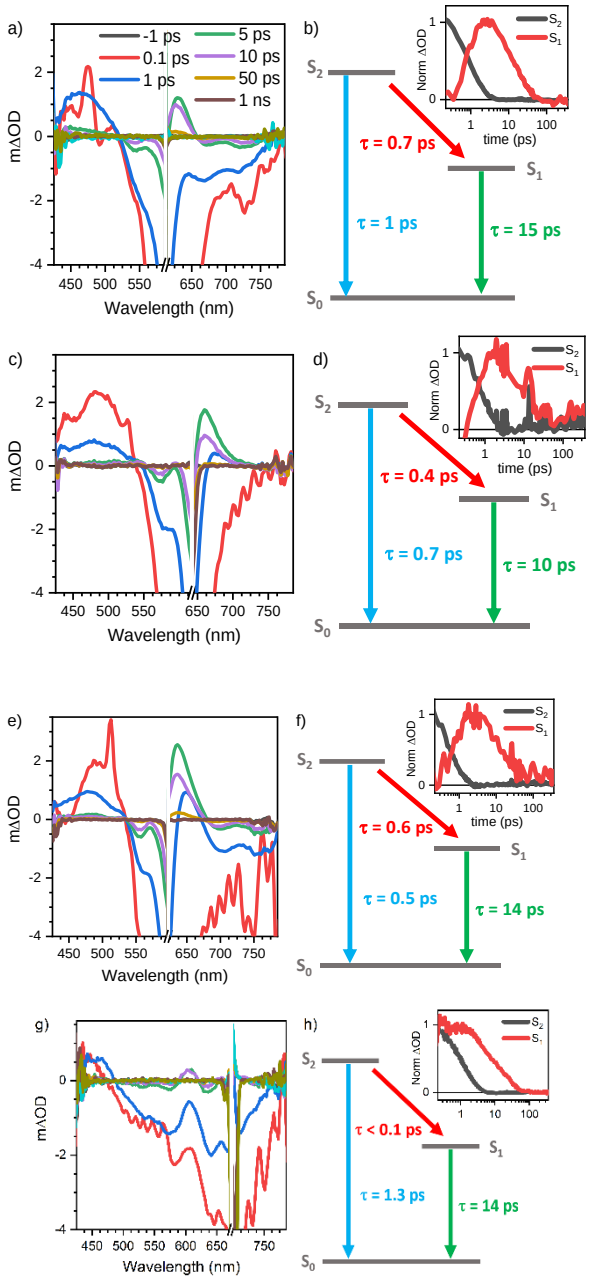

Figure S14. Femtosecond transient absorption spectra of 10 µM solution in CH_2Cl_2 of a) **DFFu**, c) **DFPy** e) **DFTh** and g) **DFThO₂** upon exciting at 600, 630 and 610 nm, respectively, with a power of 0.25 mW. Scheme of the processes taking place with their corresponding lifetime of b) **DFFu**, d) **DFPy** f) **DFTh** and h) **DFTh**. The insets include the decays obtained by global analysis of the femtosecond transient absorption data.

Femtosecond transient absorption spectroscopy (fs-TAS) was used to characterize difluorene molecules in a 10 mM solution in CH_2Cl_2. **Figure S13** shows the results for each material. As seen, there is a positive band in the 400-500 nm region that quickly decays in less than 5 ps. There is also a positive band in the 600-675 nm region that rises after few picoseconds to disappear after 50 ps. Moreover, there is a negative broad feature in the 550-750 nm region, matching the ground state absorbance, associated to the bleaching. The difference in the two positive bands kinetics indicates the presence of two different species. These species were assigned to singlets because of their short lifetimes. The kinetics of these species were energy independent (**Figure S14**), neglecting any kind of bimolecular process such as singlet-singlet annihilation. For further understanding, global analysis was performed on the femtosecond transient absorption results (see **Figure S13** insets). The global analysis shows a singlet species that quickly decays with a lifetime in the 0.4-0.7 ps range (depending on the difluorene) and another singlet species that rises in few picoseconds to decay with a lifetime of over 10 ps. These two singlets absorb in the 400-500 and 600-675 nm range, respectively. It is noticeable how the decay lifetime of the 400-500 nm singlet species was very similar to the 600-675 nm rise lifetime. The similarity in the decay and rise lifetimes indicates the transformation of one of the singlets species (S_2) into the other one (S_1). This is in agreement with previous reports, where authors found the existence of two different singlet states in structurally similar difluorenes where the first excited state (S_1) was dark and it was only populated upon energy transfer from a higher energy singlet state (S_2).

The analysis of the fs-TAS in the NIR region gave similar insights (see **Figure S15** for NIR fs-TAS results for **DFTh**). There is a broad band that absorb from 800 to 1500 composed of a band centered at 900 nm and a broader band further in the IR that decays faster. These two bands were assigned to S_1 and S_2 singlet states, respectively, as their lifetimes were identical to assignments made for the visible region.

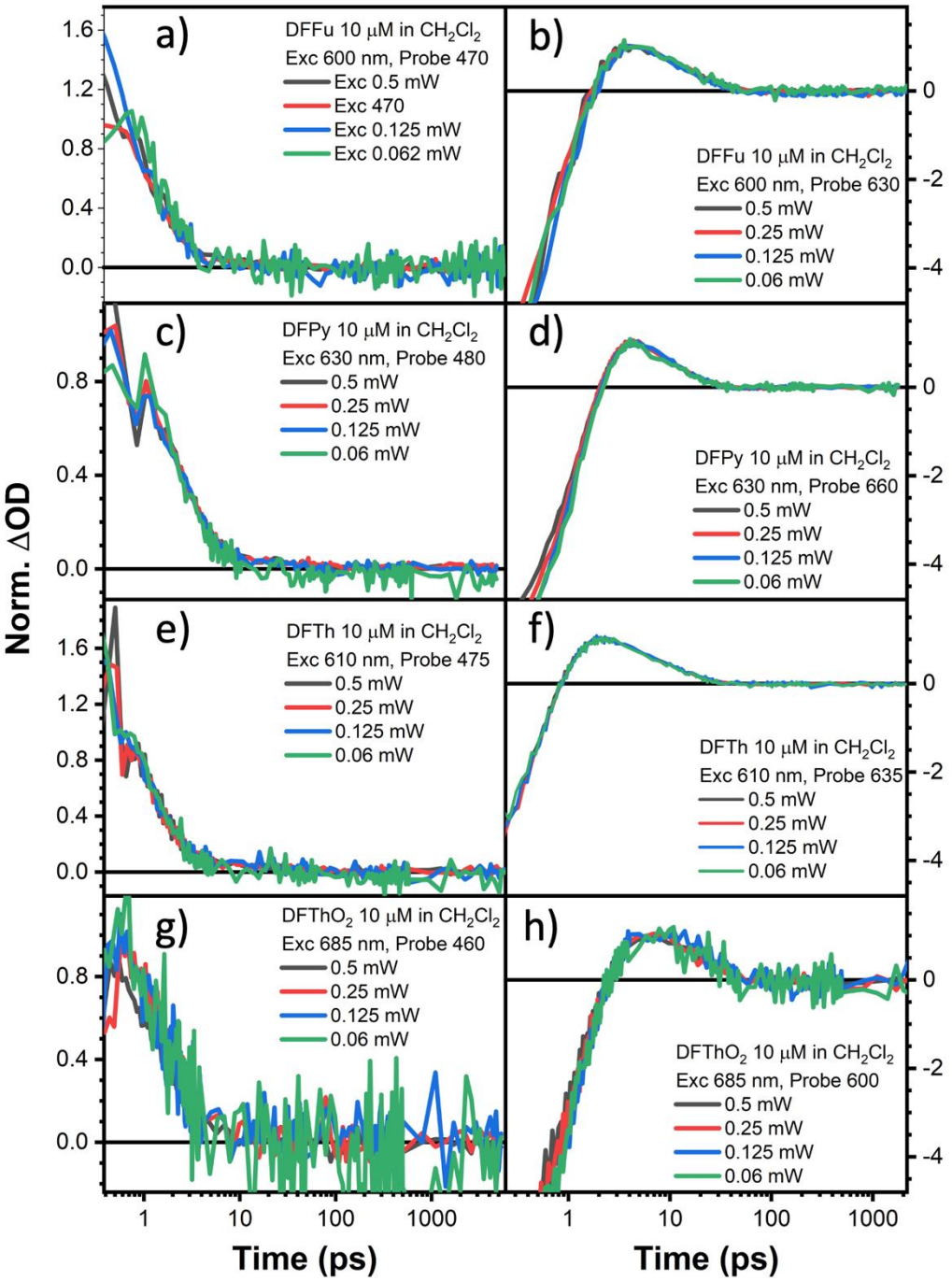

Figure S15. Transient absorption decays of **a,b) DFFu**, **c,d) DFPy**, **e,f) DFTh** and **g,h) DFTh** with excitation densities of 0.5 (black), 0.25 (red), 0.125 (blue) and 0.06 mW (green). **DFFu** was excited at 600 nm and probed at **a)** 470 and **b)** 630 nm. **DFPy** was excited at 630 and probed at **c)** 480 and **d)** 660 nm. **DFTh** was excited at 610 nm and probed at **e)** 475 and **f)** 635 nm. **$DFThO_2$** was excited at 685 nm and probed at **e)** 460 and **f)** 600 nm.

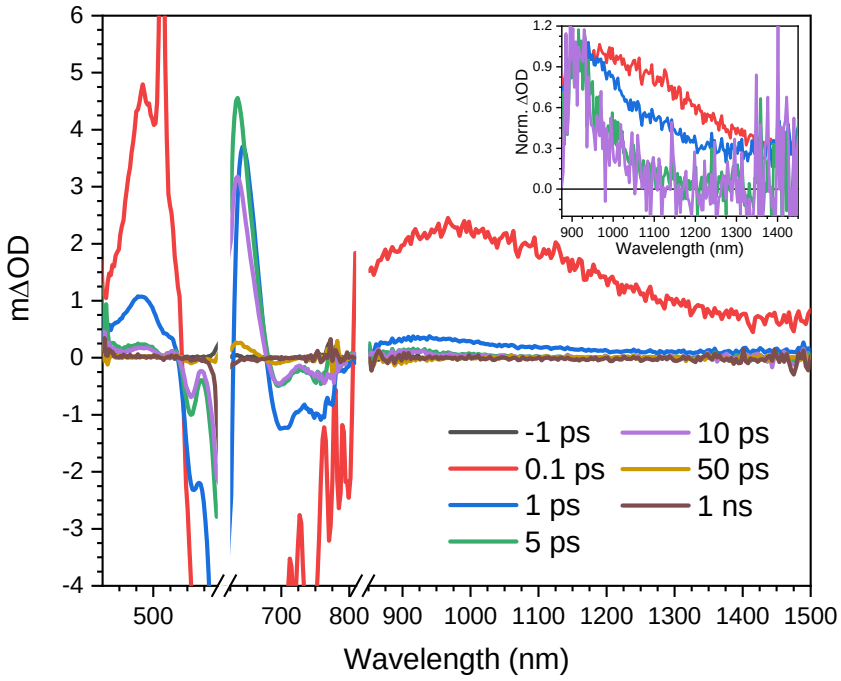

Figure S16. Femtosecond transient absorption spectra of a 10 mM **DFTh** solution in CH_2Cl_2 probed in the visible and infrared regions upon excitation at 610 nm at 0.5 mW. The inset shows the normalized spectra at 0.1, 1, 5 and 10 ps to remark the spectral evolution.

Table S5. Summary of NEVPT2 Calculation Results for Neutral **DFFu**.

State num.	NEVPT2 excitation energy (wavelength)	Oscillator strength	Dominant CASSCF configurations
0 (Ground state)	–	–	0.77504: 22220000 0.10595: 22202000 0.01547: 12211100 0.01105: 21211001
1	2.04 eV (608 nm)	0.123	0.48671: 22121000 0.16842: 21212000 0.15952: 22211000
2	2.05 eV (606 nm)	0.003	0.30544: 22202000 0.25940: 21221000 0.10424: 12221000
3	2.19 eV (566 nm)	0.856	0.61997: 22211000 0.14495: 22121000
4	2.88 eV (431 nm)	0.000	0.26359: 21221000 0.22635: 22112000 0.10405: 12221000

Electrical measurements in OFETs devices.

Bottom-gate top-contact OFETs (schematic diagram shown in **Figure S17**) were fabricated using the studied molecules as the active semiconducting layer. Gate dielectrics (d-doped Si wafers with 300 nm thermally grown SiO_2 dielectric layers) were functionalized with hexamethyldisilazane (HMDS) self-assembled monolayer. The capacitance of the 300 nm SiO_2 gate insulator was 10 $nFcm^{-2}$. Prior to the surface functionalization, the wafers were solvent cleaned by immersing them twice for 30 s each in EtOH with sonication, drying with a stream of N_2, and treating with UV-ozone for 10 min. For the HMDS treatment, the cleaned silicon wafers were exposed to HMDS vapor at room temperature in a closed air-free container under argon for one week. Next, the semiconductors were vapor-deposited on the substrates at either room temperature or preheated at 80ºC. The deposition rate was oscillating between 0.06-0.2 Å/s at a vacuum of $4{,}1x10^{-6}$ mbar. OFET devices were completed by gold vapor deposition through a shadow mask to define devices with various channel lengths and channel widths (see scheme in **Figure S17**). The devices were characterized under vacuum (in a customized probe station) and air conditions (in an EB-4 Everbeing probe station) with a 4200-SCS/C Keithley semiconductor characterization system.
Thin film layers were characterized by GIXRD and AFM measurements. AFM images were recorded by a Multimode atomic force microscope with a Nanoscope V Controller (Bruker Corporation, Billerica, MA, USA) working in tapping mode.
GIXRD data using CuKα1 radiation was recorded by using a Bruker D8 DISCOVER diffractometer. The grazing incidence X-ray diffraction setup is equipped with a parabolic Göbel mirror and a conventional line focus Cu radiation tube (40 kV/40 mA).

Device stability has been tested for a period of over 30 days and only p-type transport was registered under ambient conditions. As can be seen in the stability graphics shown in **Figure S21**, there is an initial decrease in field-effect mobility of around 20-50% of the pristine value in the first 7 days, being **DFTh** the semiconductor that best maintains the initial performance, and **DFPy** the one showing greater degradability. However, after this initial loss, the field-effect mobility is kept basically stable for over a month. Regarding the threshold voltages, they become positive after device functioning in air, probably due to doping, but remain quite low during the whole period tested. Overall, although the transistor performance is somewhat degraded under air in the first week, the semiconductors remain active and showing reasonable and stable figures of merits during the rest of the tested period.

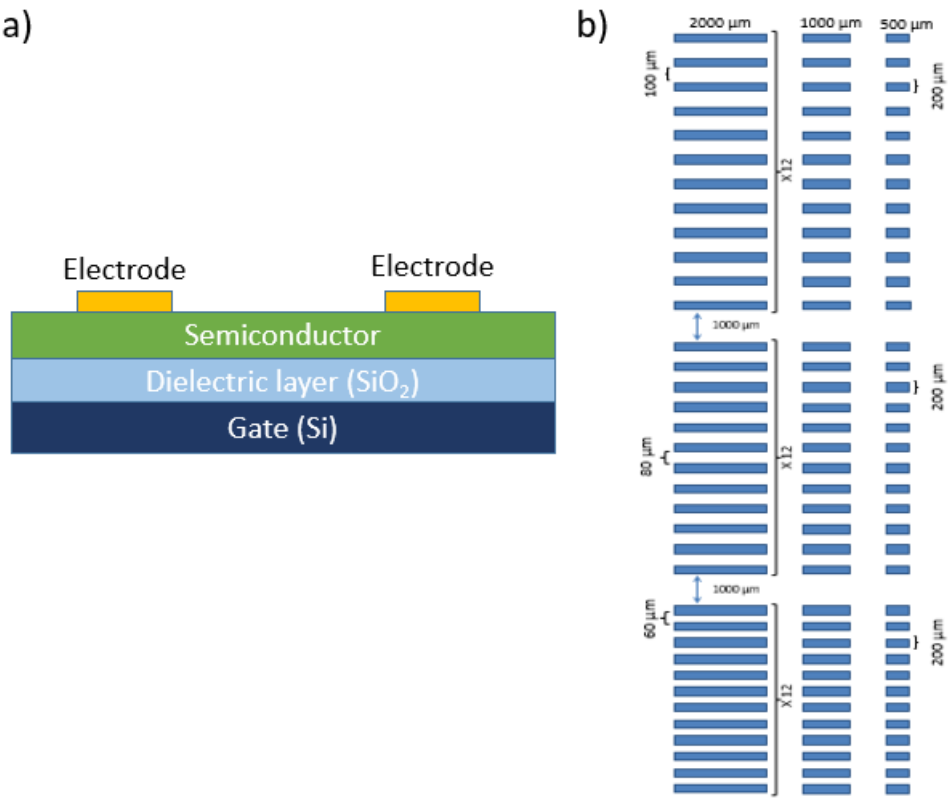

Figure S17. a) Schematic diagram of the bottom-gate top-contact OFETs used in this study. b) Scheme of the shadow masks used to define source and drain electrodes.

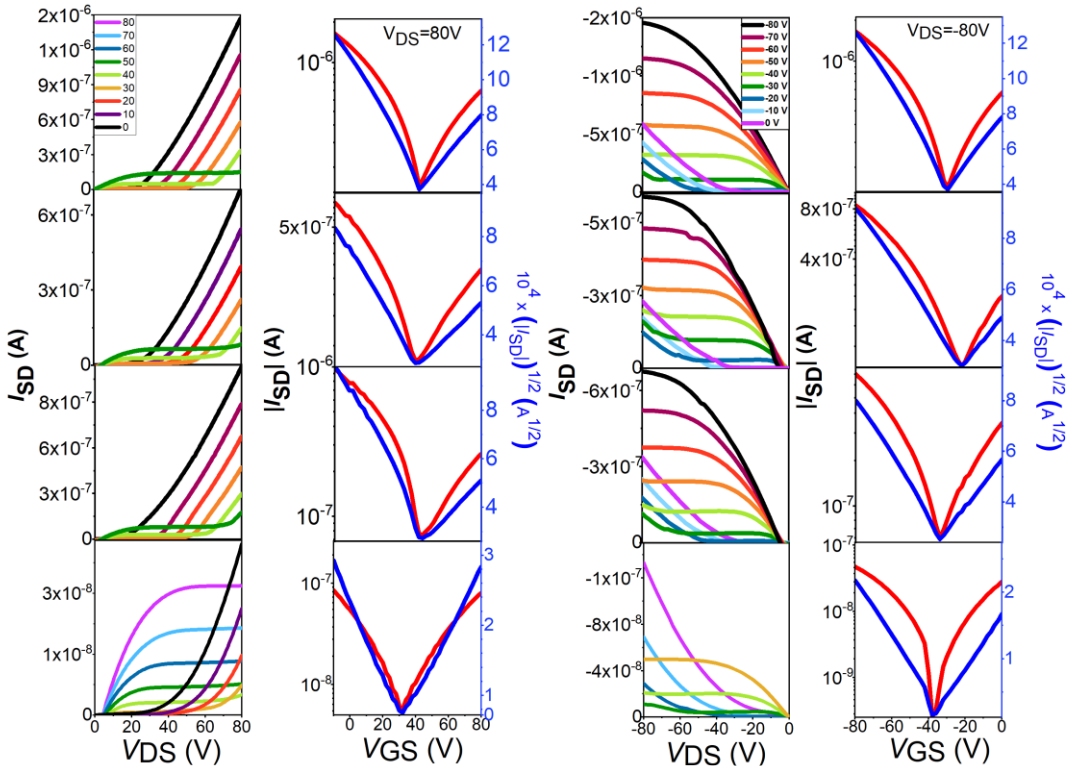

Figure S18. Output a),b),c),d) n-type, i),j),k),l) p-type, and transfer e),f),g)h) n-type, m),n),o)p) p-type characteristic curves of the fabricated OFET devices. From the bottom: **DFPy**, **DFTh**, **DFFu** and **DFThO$_2$** respectively. The organic layers were deposited on substrates preheated at 80ºC.

Table S6. Electrical measurements of the OFETs devices fabricated with semiconducting thin films deposited onto HMDS-treated substrates preheated at 80ºC. Average mobilities of at least five devices are shown.

	μ_e [$cm^2V^{-1}s^{-1}$]	V_{TH} (V)	I_{ON}/I_{OFF}
DFFu	$9x10^{-4}$ ($\pm 6x10^{-5}$)	41	$4x10^{1}$
DFTh	$6x10^{-4}$ ($\pm 3x10^{-5}$)	42	$5x10^{2}$
DFPy	$8x10^{-4}$ ($\pm 6x10^{-5}$)	30	$3x10^{1}$
$DFThSO_2$	$3x10^{-4}$ ($\pm 8x10^{-5}$)	31	$3x10^{2}$

	μ_h [$cm^2V^{-1}s^{-1}$]	V_{TH} (V)	I_{ON}/I_{OFF}
DFFu	$1x10^{-3}$ ($\pm 1x10^{-4}$)	-24	$5x10^{1}$
DFTh	$1x10^{-3}$ ($\pm 9x10^{-5}$)	-32	$1x10^{2}$
DFPy	$2x10^{-3}$ ($\pm 5x10^{-5}$)	-12	$2x10^{1}$
$DFThSO_2$	$2x10^{-4}$ ($\pm 2x10^{-5}$)	-30	$2x10^{2}$

Table S7. Electrical measurements of the OFETs devices fabricated with semiconducting thin films deposited onto HMDS-treated substrates at room temperature. Average mobilities of at least five devices are shown.

	μ_e [$cm^2V^{-1}s^{-1}$]	V_{TH} (V)	I_{ON}/I_{OFF}
DFFu	$4x10^{-4}$	31	$4x10^{1}$
DFTh	$4x10^{-4}$	30	$1x10^{3}$
DFPy	$6x10^{-4}$	40	$6x10^{1}$
$DFThSO_2$	$1x10^{-4}$	21	$6x10^{1}$

	μ_h [$cm^2V^{-1}s^{-1}$]	V_{TH} (V)	I_{ON}/I_{OFF}
DFFu	$1x10^{-3}$	-20	$7x10^{1}$
DFTh	$2x10^{-3}$	-42	$2x10^{3}$
DFPy	$1x10^{-3}$	-26	$2x10^{3}$
$DFThSO_2$	$1x10^{-4}$	-28	$2x10^{1}$

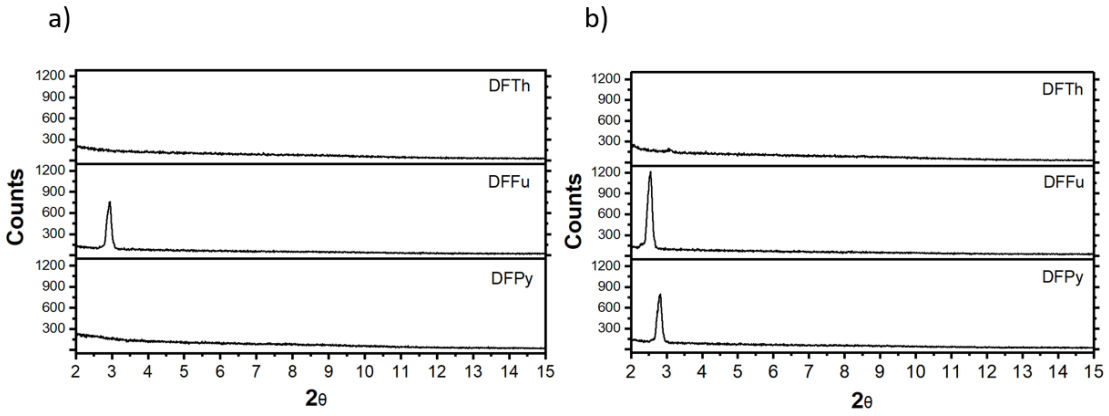

Figure S19. Θ-2Θ X-ray diffraction scans of vapor-deposited **DFTh, DFFu** and **DFPy** thin films grown on HMDS-treated Si/SiO_2 substrates a) at room temperature and b) preheated at 80ºC.

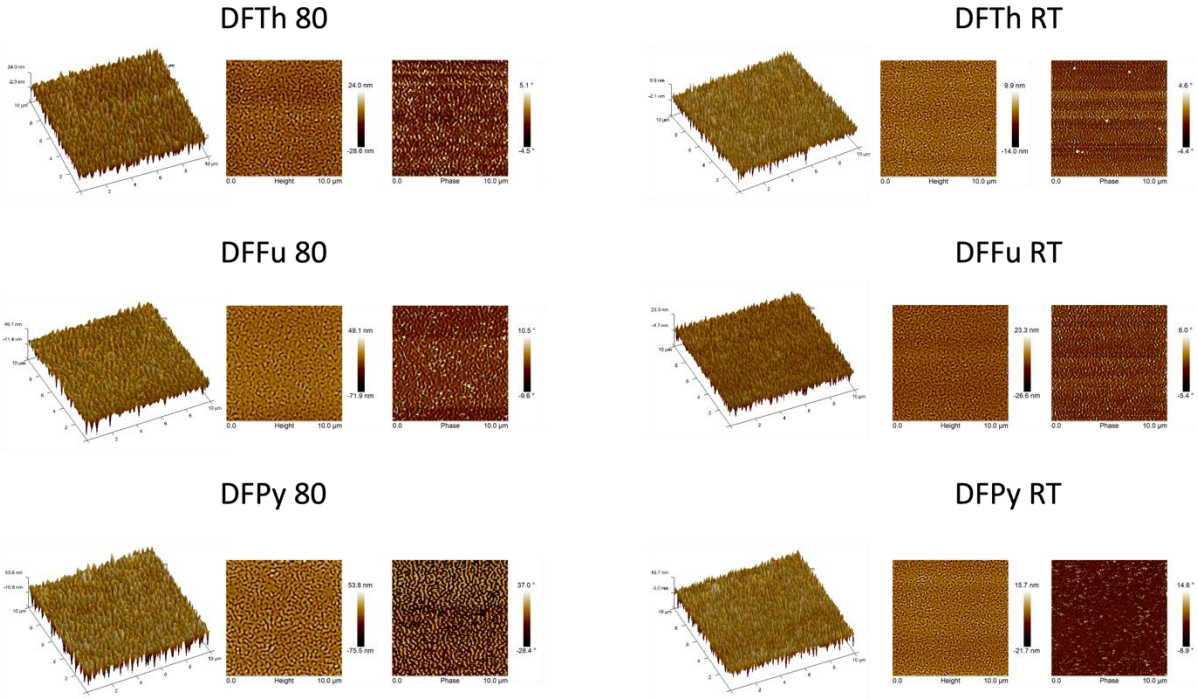

Figure S20. AFM images of semiconducting thin films deposited on substrates preheated at 80ºC and at room temperature. From the top: **DFTh**, **DFFu** and **DFPy**. Right: 80ºC and left: room temperature.

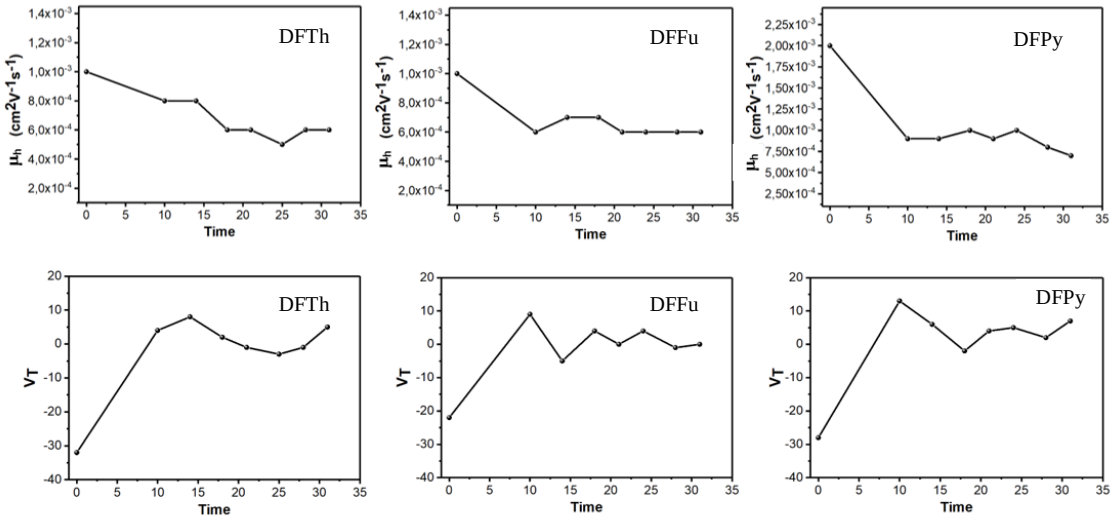

Figure S21. Variation with time in days of transistors parameters: field-effect mobilities (up) and threshold voltages (down) extracted from OFETs fabricated with semiconducting thin films deposited onto HMDS-treated substrates preheated at 80ºC.

Intramolecular reorganization energies and molecular structures

Table S8. Absolute energies of the four difluorenoheterole derivatives used to evaluate the intramolecular reorganization energy λ_i with the AP method. RB3LYP/6-311G* (for neutral system at CS geometry) and UB3LYP/6-311G* levels of theory elsewhere.

Compound→		**DFFu**	**DFTh**	**DFPy**	**DFTh(SO_2)**
Charge	**Geometry**	**Energy / a.u.**			
neutral	CS	-1772.779151	-2095.759377	-1831.536162	-2246.159801
cation	CS	-1772.560489	-2095.541239	-1831.322498	-2245.934178
cation	cation	-1772.564377	-2095.545191	-1831.325992	-2245.938987
neutral	cation	-1772.775306	-2095.755520	-1831.532691	-2246.155141
anion	CS	-1772.862355	-2095.844719	-1831.614078	-2246.254491
anion	anion	-1772.866537	-2095.849018	-1831.618614	-2246.258554
neutral	anion	-1772.775395	-2095.755522	-1831.531994	-2246.156181
neutral	BS	-1772.780871	-2095.761715	-1831.537117	-2246.163006
cation	BS	-1772.562467	-2095.543337	-1831.324257	-2245.936759
neutral	cation	-1772.778947	-2095.759853	-1831.535428	-2246.160732
anion	BS	-1772.864350	-2095.846861	-1831.615999	-2246.256629
neutral	anion	-1772.778855	-2095.759709	-1831.534737	-2246.161166

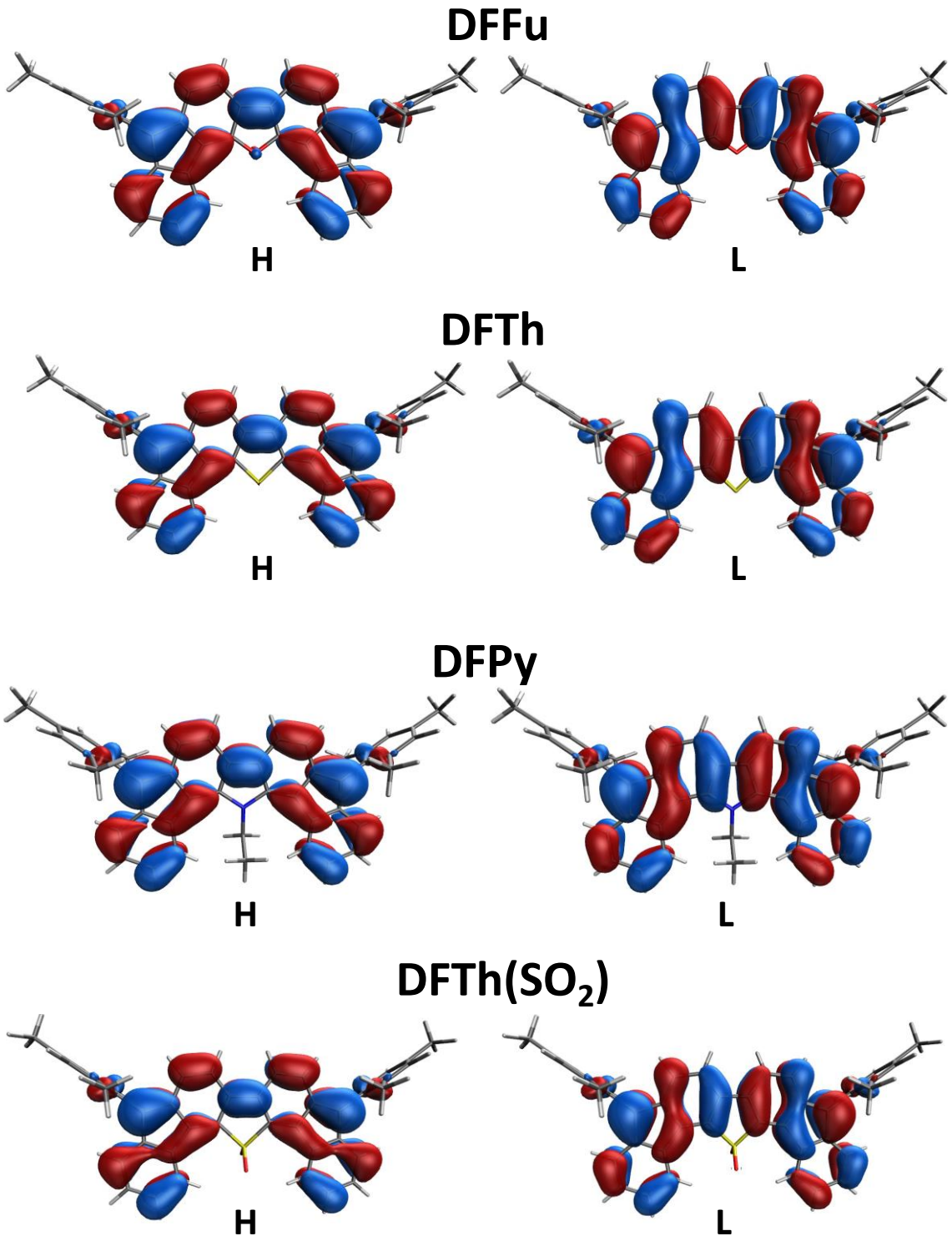

Figure S22. HOMO and LUMO of the four difluorenoheterole derivatives, calculated at RB3LYP/6-311G* level (CS structures).

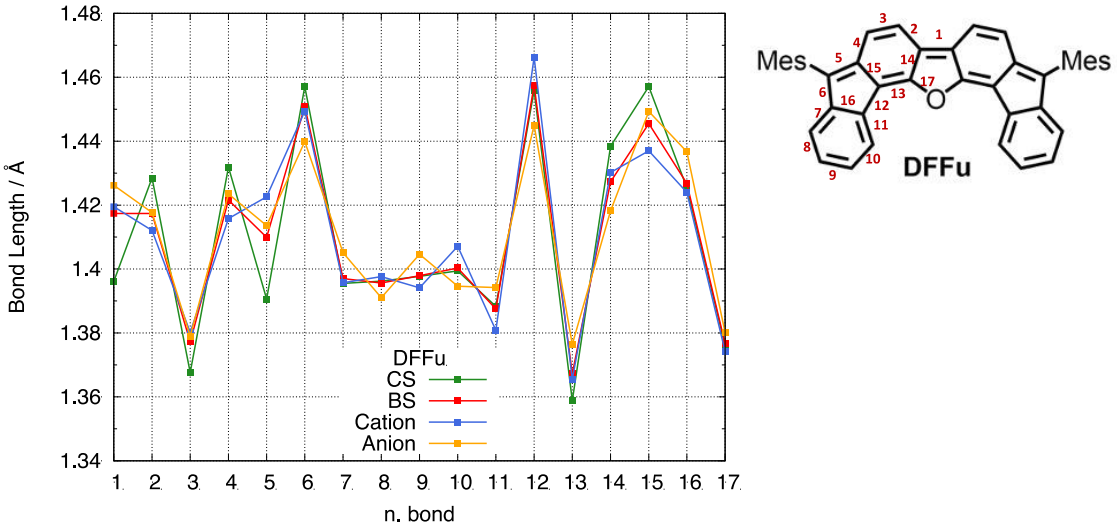

Figure S23. Bond lengths of **DFFu** calculated at CS (green), BS (red), cation (blue) and anion (orange) geometries. Top right: the definition of chosen bonds. The CS geometry is calculated with RB3LYP functional, while other geometries are obtained with UB3LYP functional. The 6-311G* basis set is used.

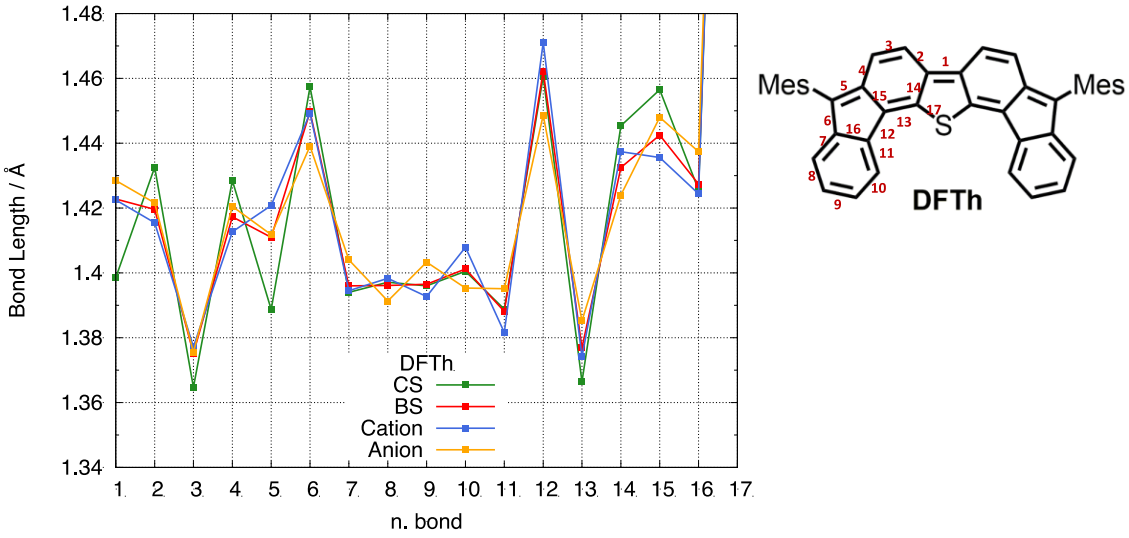

Figure S24. Bond lengths of **DFTh** calculated at CS (green), BS (red), cation (blue) and anion (orange) geometries. Top right: the definition of chosen bonds. The CS geometry is calculated with RB3LYP functional, while other geometries are obtained with UB3LYP functional. The 6-311G* basis set is used.

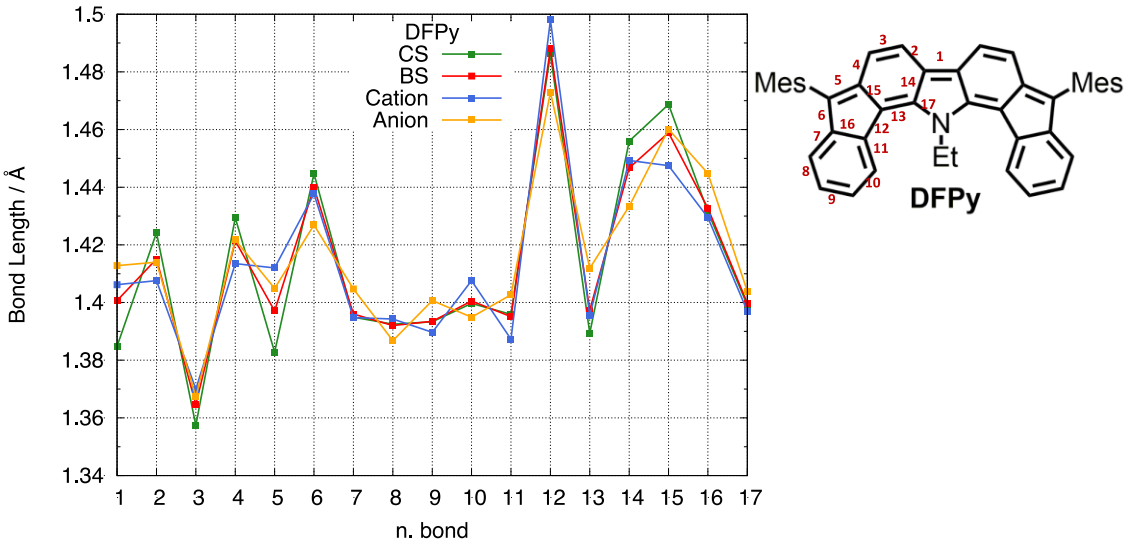

Figure S25. Bond lengths of **DFPy** calculated at CS (green), BS (red), cation (blue) and anion (orange) geometries. Top right: the definition of chosen bonds. The CS geometry is calculated with RB3LYP functional, while other geometries are obtained with UB3LYP functional. The 6-311G* basis set is used.

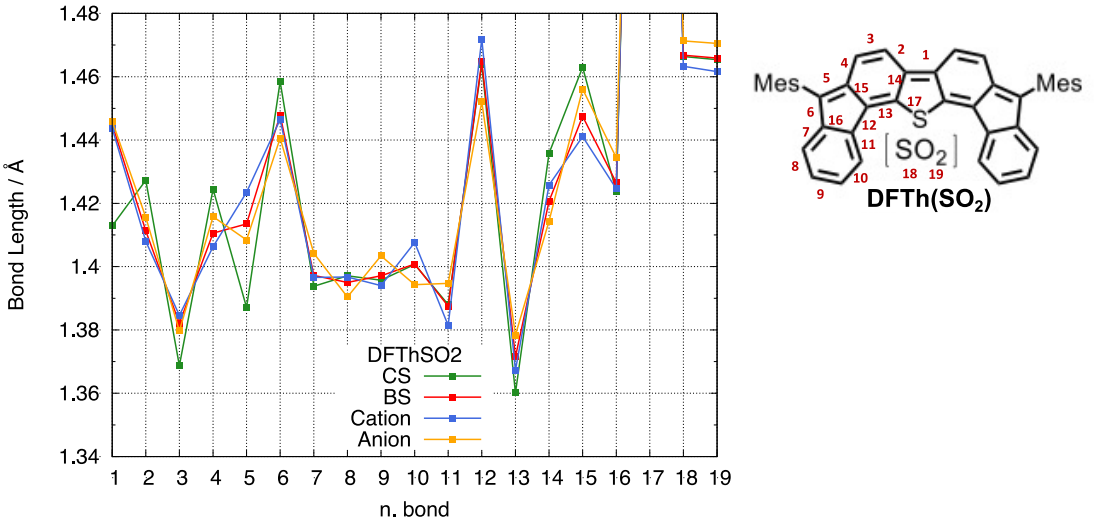

Figure S26. Bond lengths of **DFTh(SO_2)** calculated at CS (green), BS (red), cation (blue) and anion (orange) geometries. Top right: the definition of chosen bonds. Bond number 17 is the C-S bond which is 1.80Å for all geometries. The CS geometry is calculated with RB3LYP functional, while other geometries are obtained with UB3LYP functional. The 6-311G* basis set is used.

References

[1] S. J. Malthus, S. A. Cameron, S. Brooker, *Inorg. Chem.* **2018**, *57*, 2480.
[2] CrysAlisPro; Rigaku OD, The Woodlands, TX, 2015.
[3] O. V. Dolomanov, L. J. Bourhis, R. J. Gildea, J. A. K. Howard, H. Puschmann, *J. Appl. Cryst.* **2009**, *42*, 339.
[4] G. M. Sheldrick, *Acta Crystallogr., Sect. A* **2015**, *71*, 3.
[5] G. M. Sheldrick, *Acta Crystallogr., Sect. C* **2015**, *71*, 3.
[6] Y. Shao, M. Head-Gordon, A. I. Krylov, *J. Chem. Phys.* **2003**, *118*, 4807.
[7] (a) F. Wang, T. Ziegler, *J. Chem. Phys.* **2004**, *121*, 12191. (b) F. Wang, T. Ziegler, *J. Chem. Phys.* **2005**, *122*, 074109. c) F. Wang, T. Ziegler, *Int. J. Quantum Chem.* **2006**, *106*, 2545.
[8] (a) E. F. Hayes, A. K. Q. Siu, *J. Am. Chem. Soc.* **1971**, *93*, 2090; (b) K. Yamaguchi, *Chem. Phys. Lett.* **1975**, 33, 330.
[9] H. Hayashi, J. E. Barker, A. Cárdenas Valdivia, R. Kishi, S. N. MacMillan, C. J. Gómez-García, H. Miyauchi, Y. Nakamura, M. Nakano, S.-i. Kato, M. M. Haley, J. Casado, *J. Am. Chem. Soc.* **2020**, *142*, 20444.
[10] Z. Chen, C. S. Wannere, C. Corminboeuf, R. Puchta, P. v. R. Schleyer, *Chem. Rev.* **2005**, *105*, 3842.
[11] D. Geuenich, K. Hess, F. Köhler, R. Herges, *Chem. Rev.* **2005**, *105*, 3758.
[12] H. Iikura, T. Tsuneda, T. Yanai, K. Hirao, *J. Chem. Phys.* **2001**, *115*, 3540.
[13] T. Stein, H. Eisenberg, L. Kronik, R. Baer, *Phys. Rev. Lett.* **2010**, *105*, 266802.
[14] (a) C. Angeli, R. Cimiraglia, S. Evangelisti, T. Leininger, J.-P. Malrieu, *J. Chem. Phys.* **2001**, *114*, 10252. (b) C. Angeli, R. Cimiraglia, J.-P. Malrieu, *Chem. Phys. Lett.* **2001**, *350*, 297. (c) C. Angeli, R. Cimiraglia, J.-P. Malrieu, *J. Chem. Phys.* **2002**, *117*, 9138.
[15] G. L. Stoychev, A. A. Auer, F. Neese, *J. Chem. Theory Comput.* **2017**, *13*, 554.
[16] (a) H. Oberhofer, K. Reuter, J. Blumberger, *Chem. Rev.* **2017**, *117*, 10319; (b) J.-L. Brédas, D. Beljonne, V. Coropceanu, J. Cornil, *Chem. Rev.* **2004**, *104*, 4971; (c) V. Coropceanu, J. Cornil, D. da Silva Filho, Y. Olivier, R. Silbey, J.-L. Brédas, *Chem. Rev.* **2007**, *107*, 926.
[17] (a) S. Canola, C. Pecoraro, F. Negri, *Chem. Phys.* **2016**, *478*, 130; (b) A. Troisi, G. Orlandi, *Chem. Phys. Lett.* **2001**, *344*, 509; (c) K. Senthilkumar, F. C. Grozema, F. M. Bickelhaupt, L. D. A. Siebbeles, *J. Chem. Phys.* **2003**, *119*, 9809; (d) J. E. Norton, J.-L. Brédas, *J. Chem. Phys.* **2008**, *128*, 034701; (e) G. Ricci, S. Canola, Y. Dai, D. Fazzi, F. Negri, *Molecules* **2021**, *26*, 4119.
[18] (a) B. Baumeier, J. Kirkpatrick, D. Andrienko, *Phys. Chem. Chem. Phys.* **2010**, *12*, 11103; (b) E. F. Valeev, V. Coropceanu, D. da Silva Filho, S. Salman, J.-L. Brédas, *J. Am. Chem. Soc.* **2006**, *128*, 9882.
[19] C. Schober, K. Reuter, H. Oberhofer, *J. Chem. Phys.* **2016**, *144*, 054103.
[20] Y. Shao, Z. Gan, E. Epifanovsky, A. T. B. Gilbert, M. Wormit, J. Kussmann, A. W. Lange, A. Behn, J. Deng, X. Feng, D. Ghosh, M. Goldey P. R. Horn, L. D. Jacobson, I. Kaliman, R. Z. Khaliullin, T. Kús, A. Landau, J. Liu, E. I. Proynov, Y. M. Rhee, R. M. Richard, M. A. Rohrdanz, R. P. Steele, E. J. Sundstrom, H. L. Woodcock III, P. M. Zimmerman, D. Zuev, B. Albrecht, E. Alguire, B. Austin, G. J. O. Beran, Y. A. Bernard, E. Berquist, K. Brandhorst, K. B. Bravaya, S. T. Brown, D. Casanova, C.-M. Chang, Y. Chen, S. H. Chien, K. D. Closser, D. L. Crittenden, M. Diedenhofen, R. A. DiStasio Jr., H. Dop, A. D. Dutoi, R. G. Edgar, S. Fatehi, L. Fusti-Molnar, A. Ghysels, A. Golubeva-Zadorozhnaya, J. Gomes, M.

W. D. Hanson-Heine, P. H. P. Harbach, A. W. Hauser, E. G. Hohenstein, Z. C. Holden, T.-C. Jagau, H. Ji, B. Kaduk, K. Khistyaev, J. Kim, J. Kim, R. A. King, P. Klunzinger, D. Kosenkov, T. Kowalczyk, C. M. Krauter, K. U. Lao, A. Laurent, K. V. Lawler, S. V. Levchenko, C. Y. Lin, F. Liu, E. Livshits, R. C. Lochan, A. Luenser, P. Manohar, S. F. Manzer, S.-P. Mao, N. Mardirossian, A. V. Marenich, S. A. Maurer, N. J. Mayhall, C. M. Oana, R. Olivares-Amaya, D. P. O'Neill, J. A. Parkhill, T. M. Perrine, R. Peverati, P. A. Pieniazek, A. Prociuk, D. R. Rehn, E. Rosta, N. J. Russ, N. Sergueev, S. M. Sharada, S. Sharmaa, D. W. Small, A. Sodt, T. Stein, D. Stück, Y.-C. Su, A. J. W. Thom, T. Tsuchimochi, L. Vogt, O. Vydrov, T. Wang, M. A. Watson, J. Wenzel, A. White, C. F. Williams, V. Vanovschi, S. Yeganeh, S. R. Yost, Z.-Q. You, I. Y. Zhang, X. Zhang, Y. Zhou, B. R. Brooks, G. K. L. Chan, D. M. Chipman, C. J. Cramer, W. A. Goddard III, M. S. Gordon, W. J. Hehre, A. Klamt, H. F. Schaefer III, M. W. Schmidt, C. D. Sherrill, D. G. Truhlar, A. Warshel, X. Xua, A. Aspuru-Guzik, R. Baer, A. T. Bell, N. A. Besley, J.-D. Chai, A. Dreuw, B. D. Dunietz, T. R. Furlani, S. R. Gwaltney, C.-P. Hsu, Y. Jung, J. Kong, D. S. Lambrecht, W. Liang, C. Ochsenfeld, V. A. Rassolov, L. V. Slipchenko, J. E. Subotnik, T. Van Voorhis, J. M. Herbert, A. I. Krylov, P. M. W. Gill, and M. Head-Gordon, *Mol. Phys.* **2015**, *113*, 184.

[21] F. Neese, "Software update: the ORCA program system, version 4.0" *Wiley Interdisciplinary Reviews: Computational Molecular Science*, **2017**, Vol. 8, Issue 1, p. e1327.

[22] M. J. Frisch, G. W. Trucks, H. B. Schlegel, G. E. Scuseria, M. A. Robb, J. R. Cheeseman, G. Scalmani, V. Barone, B. Mennucci, G. A. Petersson, H. Nakatsuji, M. Caricato, X. Li, H. P. Hratchian, A. F. Izmaylov, J. Bloino, G. Zheng, J. L. Sonnenberg, M. Hada, M. Ehara, K. Toyota, R. Fukuda, J. Hasegawa, M. Ishida, T. Nakajima, Y. Honda, O. Kitao, H. Nakai, T. Vreven, J. A., J. Montgomery, J. E. Peralta, F. Ogliaro, M. Bearpark, J. J. Heyd, E. Brothers, K. N. Kudin, V. N. Staroverov, R. Kobayashi, J. Normand, K. Raghavachari, A. Rendell, J. C. Burant, S. S. Iyengar, J. Tomasi, M. Cossi, N. Rega, J. M. Millam, M. Klene, J. E. Knox, J. B. Cross, V. Bakken, C. Adamo, J. Jaramillo, R. Gomperts, R. E. Stratmann, O. Yazyev, A. J. Austin, R. Cammi, C. Pomelli, J. W. Ochterski, R. L. Martin, K. Morokuma, V. G. Zakrzewski, G. A. Voth, P. Salvador, J. J. Dannenberg, S. Dapprich, A. D. Daniels, Ö. Farkas, J. B. Foresman, J. V. Ortiz, J. Cioslowski, D. J. Fox, Gaussian 09 Revision D.01, Gaussian, Inc. Wallingford CT, 2009.

[23] Frisch, M.J.; Trucks, G.W.; Schlegel, H.B.; Scuseria, G.E.; Robb, M.A.; Cheeseman, J.R.; Scalmani, G.; Barone, V.; Petersson, G.A.; Nakatsuji, H.; Li, X.; Caricato, M.; Marenich, A.V.; Bloino, J.; Janesko, B.G.; Gomperts, R.; Mennucci, B.; Hratchian, H. P.; Ortiz, J. V.; Izmaylov, A. F.; Sonnenberg, J. L.; Williams-Young, D.; Ding, F.; Lipparini, F.; Egidi, J.; Goings, J.; Peng, B.; Petrone, A.; Henderson, T.; Ranasinghe, D.; Zakrzewski, V. G.; Gao, J.; Rega, N.; Zheng, G.; Liang, W.; Hada, M.; Ehara, M.; Toyota, K.; Fukuda, R.; Hasegawa, J.; Ishida, M.; Nakajima, T.; Honda, Y.; Kitao, O.; Nakai, H.; Vreven, T.; Throssell, K.; Montgomery, Jr. J. A.; Peralta, J. E.; Ogliaro, F.; Bearpark, M. J.; Heyd, J. J.; Brothers, E. N.; Kudin, K. N.; Staroverov, V. N.; Keith, T. A.; Kobayashi, R.; Normand, J.; Raghavachari, K.; Rendell, A. P.; Burant, J. C.; Iyengar, S. S.; Tomasi, J.; Cossi, M.; Millam, J. M.; Klene, M.; Adamo, C.; Cammi, R.; Ochterski, J. W.; Martin, R. L.; Morokuma, K.; Farkas, O.; Foresman, J. B.; Fox, J. D. Gaussian 16 Revision A.01. Gaussian, Inc., Wallingford CT, 2016